Multi-objective optimal power flow of thermal-wind-solar power system using an adaptive geometry estimation based multi-objective differential evolution

Truong Hoang Bao Huy [a], Hien Thanh Doan [b], Dieu Ngoc Vo [c,d], Kyu-haeng Lee [e,*], Daehee Kim [a,*]

[a] Department of Future Convergence Technology, Soonchunhyang University, Asan-si, Chuncheongnam-do 31538, South Korea
[b] Department of Electronic Engineering, Sogang University, Mapo-gu, Seoul, South Korea
[c] Department of Power Systems, Ho Chi Minh City University of Technology (HCMUT), 268 Ly Thuong Kiet Street, District 10, Ho Chi Minh City, Viet Nam
[d] Vietnam National University Ho Chi Minh City, Linh Trung Ward, Thu Duc City, Ho Chi Minh City, Viet Nam
[e] Department of Mobile Systems Engineering, Dankook University, Yongin-si, 16890 Gyeonggi-do, South Korea

HIGHLIGHTS

- Multi-objective optimal power flow of thermal-wind-solar power system is formulated.
- Uncertainties of wind and solar irradiance distribution are simulated using different probability density functions.
- An adaptive geometry estimation based multi-objective differential evolution is proposed.
- Various case studies with combinations of two-, three-, or four-objective optimization are performed.
- The superiority of the proposed method over other state-of-the-art algorithms is confirmed.

ARTICLE INFO

ABSTRACT

Sustainable energy is a key component of sustainable development. The current grid can be supplied by fossil fuel generators and renewable energy sources (RESs)-based generators, such as solar photovoltaic (PV) and wind power generators. In an electrical network, power generation from several sources must be optimally coordinated to ensure efficient and economical operation. However, the intermittent and uncertain nature of RESs complicate the operation of power systems. In this study, an adaptive geometry estimation-based multi-objective differential evolution (AGE-MODE) method is proposed for multi-objective optimal power flow in a hybrid power system of thermal, wind, and solar energy sources (MOOPF-TWS). In the proposed approach, wind and solar PV power outputs are predicted based on Weibull and lognormal probability distribution functions, respectively. Therefore, the generation costs for solar and wind power can be divided into direct costs, penalty costs for underestimation, and reserve costs for overestimation. Furthermore, the emissions, voltage deviation, and real power loss are considered in particular cases. AGE-MODE is applied to modified IEEE 30-bus and 57-bus systems, where different case studies are simulated with combinations of two-, three-, and four-objective optimizations in MOOPF-TWS problems. Comparisons between AGE-MODE and other recently developed multi-objective methods demonstrate its effectiveness in resolving MOOPF-TWS problems, particularly for cases with more than two objectives.

1. Introduction

Optimal power flow (OPF) is critical for maintaining the reliable and economical operation of deregulated power grids. The OPF can be expressed as a single-objective or multi-objective framework aimed at minimizing the generation cost, emissions, voltage deviation, and transmission losses, with constraints related to the power flow equations, equipment operating limits, and system security. The OPF problem defines the optimal operating state of the power system and the

* Corresponding authors.
E-mail addresses: kyuhaeng.lee@dankook.ac.kr (K.-h. Lee), daeheekim@sch.ac.kr (D. Kim).

Nomenclature

a_k, b_k, c_k	cost coefficients of the kth thermal power unit
$C_{s,j}, C_{Rs,j}, C_{Ps,j}$	direct cost, reserve cost, and penalty cost of the jth solar PV power plant
C_{TP}	fuel cost of thermal power units
$C_{w,i}, C_{Rw,i}, C_{Pw,i}$	direct cost, reserve cost, and penalty cost of the ith wind power plant
d_k, e_k	coefficients representing the valve-point effects of the kth thermal power unit
$E(P_{sav,j} < P_{ss,j})$	expectation of solar PV power lower than the scheduled power
$E(P_{sav,j} > P_{ss,j})$	expectation of solar PV power higher than the scheduled power
$f_s(P_{sav,j} < P_{ss,j})$	likelihood of shortfall of solar PV power
$f_s(P_{sav,j} > P_{ss,j})$	likelihood of an excess of solar PV power
$f_w(p_{w,i})$	probability distribution function of the ith wind power plant
G_{ij}, B_{ij}	transfer conductance and susceptance between the ith bus and j^{th} bus
$G_{n(ij)}$	transfer conductance of the nth branch connecting i^{th} bus and j^{th} bus
G_s	solar irradiance
G_{std}	solar irradiance in the standard environment
$g(x,u)$	set of inequality constraints
$h(x,u)$	set of equality constraints
$K_{Ds,j}, K_{Rs,j}, K_{Ps,j}$	direct cost, reserve cost, and penalty cost coefficients of the jth solar PV power plant
$K_{Dw,i}, K_{Rw,i}, K_{Pw,i}$	direct cost, reserve cost, and penalty cost coefficients of the ith wind power plant
N_B	number of buses
N_C	number of VAR compensators
N_D	number of load buses
N_G	number of generation buses
N_{SP}	number of solar PV power plants
N_{TP}	total number of thermal power units
N_{WP}	number of wind power plants
N_L	number of transmission lines
N_T	number of regulating transformers
P_D, Q_D	real and reactive power demands
P_G, Q_G	real and reactive power generation from power sources (thermal, wind, and solar)
$P_{TP,1}$	real power generation of the reference bus
P_{sr}	rated power of solar PV
$P_{sav,j}$	actual available power of the jth solar PV power plant
$P_{ss,j}$	scheduled power of the jth solar PV power plant
$P_{TP,k}$	real power output of the kth thermal power unit
$P_{wav,i}$	actual available power of the ith wind power plant
$P_{wr,i}$	rated power of the ith wind power plant
p_{wr}	rated power of a wind turbine
$P_{ws,i}$	scheduled power of the ith wind power plant
Q_C	shunt VAR compensation
R_c	certain irradiance point
S_L	transmission line loading
T	transformer tap setting
u, x	vectors of control and state variables
VD	voltage deviation
V_G	generation bus voltage magnitude
V_i	voltage magnitude at i^{th} bus
V_L	load bus voltage magnitude
α, β	scale and shape factors of the Weibull probability distribution function
δ_{ij}	difference in voltage angles between the ith bus and j^{th} bus
$\alpha_k, \beta_k, \gamma_k, \omega_k, \mu_k$	coefficients of emission of the kth thermal power unit
$\lambda_P, \lambda_Q, \lambda_V, \lambda_S$	penalty factors for the inequality constraints
μ, σ	mean and standard deviation of the lognormal probability distribution function
υ	wind speed
$\upsilon_{in}, \upsilon_{out}, \upsilon_r$	cut-in speed, cut-out speed, and rated speed of a wind turbine

corresponding settings of the control variables, active power output, generator voltage magnitude, shunt compensators, and transformer tap settings. The traditional OPF problem, which considers only fossil fuel energy sources, is essentially a large-scale, multidimensional, non-convex, nonlinear, and complex optimization problem. Renewable energy sources (RESs) are becoming increasingly important to mitigate the environmentally harmful impacts of traditional energy sources. As some of the fastest-growing clean energy sources, solar and wind energy sources have steadily increased worldwide over the past few decades. Despite the inherent advantages of pollution reduction and resource conservation, the uncertain nature of power production from RESs may pose difficulties in the operation and distribution of the power system. The optimal dispatch of these sources is the key to their successful integration into a secure and profitable grid and electricity market. Therefore, the OPF problem must be extended to consider the stochastic nature of wind and solar energies when integrating these intermittent energy sources into a grid.

Over the past few decades, researchers have extensively studied solutions to traditional OPF problems using only thermal power generators. Numerous evolutionary algorithms (EAs) have been developed with the advancement of soft computing. These methods have the advantage of being less susceptible to the specific characteristics of the problems and can handle large-scale search spaces. Moreover, the population-based nature of these algorithms enables them to simultaneously estimate multiple points in a search domain. Therefore, EAs can effectively solve OPF problems. Some of the latest applications of EAs to traditional OPF problems include differential evolution (DE) [1–3],

moth swarm algorithm (MSA) [4,5], most valuable player algorithm (MVPA) [6], biogeography-based optimization (BBO) [7], grey wolf optimizer (GWO) [8], and salp swarm optimization (SSO) [9].

In the aforementioned studies, the OPF was constructed as a single-objective problem, and different objective functions were aggregated into a single-objective function. Although these approaches are simple, they cannot represent a reasonable trade-off between objective functions when all the objective functions are important. Therefore, researchers have focused on multi-objective OPF (MOOPF) problems to provide compromise solutions among different objective functions, namely generation costs, emissions, voltage deviation, and transmission losses. Multi-objective EAs (MOEAs) have been evaluated as suitable for multi-objective problems [10]. Without aggregating objective functions, MOEAs can solve multi-objective functions simultaneously in a single run. There have been significant developments in the studies and applications of MOEAs to the MOOPF problem, such as the multi-objective search group algorithm (MOSGA) [11], non-dominated sorting genetic algorithm III (NSGA-III) [12], hybrid SSO and particle swarm optimizer (HSSO-PSO) [13], multi-objective beetle antennae search (NMBAS) [14], multi-objective jellyfish search (MOJFS) [15], MOEA based on decomposition (MOEA/D) [16], improved heap-based optimization algorithm (IHOA) [17], modified hybrid beetle antennae search (MHBAS) [18], and multi-objective manta ray foraging optimizer (MOMRFO) [19].

Recently, RESs have been widely used in electric power systems. Researchers have expanded the OPF problem to consider systems that include thermal power and RESs. To solve the OPF framework, Biswas

Table 1

Brief comparison of the reviewed references and current study on MOOPF problems incorporating with RESs.

Refs.	Objective functions				RESs		Systems	Approach	Solution method
	Cost	Emission	Loss	Voltage deviation	Wind	Solar			
[20]	√	√	-	-	√	√	30-bus	weighted metric	SHADE-SF
[21]	√	-	√	√	√	√	30-bus	weighted metric	PPSOGSA
[22]	√	-	√	√	√	-	30-bus, 118-bus	weighted metric	MMSA
[23]	√	√	√	√	√	-	30-bus, 57-bus	weighted metric	CPSOGSA
[24]	√	√	-	-	√	√	30-bus, 57-bus, 118-bus	weighted metric	HMICA-SQP
[25]	√	√	-	-	√	√	30-bus, 57-bus, 118-bus	weighted metric	DEEPSO
[26]	√	√	√	√	√	√	30-bus	weighted metric	FDBAGDE
[27]	√	√	√	√	√	-	30-bus, 57-bus, 118-bus	weighted metric	COA
[28]	√	√	√	-	√	√	30-bus, 57-bus	weighted metric	BMO
[29]	√	√	√	-	√	√	30-bus	weighted metric	GWO
[30]	√	√	√	√	√	√	30-bus	weighted metric	AFDB-SFS
[31]	-	-	√	√	√	√	57-bus	weighted metric	MRUN
[32]	√	-	√	√	√	-	30-bus	MOEAs	NSPSO
[33]	√	-	√	√	√	-	30-bus, 300-bus	MOEAs	MOGWO
[34]	√	√	-	-	√	√	30-bus	MOEAs	MOEA/D, SMODE
[35]	√	-	-	-	√	√	30-bus	MOEAs	CMOPEO
[36]	√	-	√	√	√	√	30-bus	MOEAs	MOAGDE
[37]	√	√	√	√	√	√	30-bus	MOEAs	ACNSDE
[38]	√	√	√	√	√	√	30-bus, 57-bus	MOEAs	MOSGA
[39]	√	√	-	-	√	-	30-bus	MOEAs	MOQILDE
[40]	√	√	√	√	√	√	30-bus	MOEAs	MOPFA
Present study	√	√	√	√	√	√	30-bus, 57-bus	MOEAs	AGE-MODE

et al. [20] proposed a hybrid system comprising three thermal generation units, a solar photovoltaic (PV) farm, and two wind farms. The costs of the solar and wind generators added penalty and reserve costs for underestimation and overestimation, respectively. The total operational costs and carbon taxes of various power sources were resolved as a single-objective model using a successful history-based adaptation of DE and the superiority of feasible solutions (SHADE-SF). Ullah et al. [21] addressed an optimum generation scheduling problem by combining solar and wind power systems using a fusion of phasor PSO and the gravitational search algorithm (PPSOGSA). The author in [22] performed optimal scheduling with combined heat and power along with wind power, wherein a modified moth swarm optimizer algorithm (MMSA) was used to resolve the scheduling problem. FACTS devices were investigated in [23] for a system involving thermal and wind generation, and the OPF framework was resolved based on a chaotic PSOGSA. OPF solutions with numerous energy sources were studied using a hybrid modified imperialist competitive algorithm and sequential quadratic programming (HMICA-SQP) in [24]. In [25], the authors combined PSO and the DE method (DEEPSO) to resolve a stochastic OPF by considering controllable solar and wind energies in 30-, 57-, and 118-bus networks. In another study, a fusion of the fitness–distance balance (FDB) and adaptive guided DE (AGDE) was performed to resolve the OPF problem in a 30-bus network connected to wind and solar power [26]. The FDBAGDE was validated using benchmark functions and OPF planning, which proved its effectiveness in determining the optimal solution. An OPF with thermal-wind energies was proposed in [27] using the coyote optimizer algorithm (COA), wherein a single-objective problem was formed by transforming the multi-objective problem. Sulaiman et al. [28] applied a barnacles mating optimizer (BMO) to resolve the OPF framework in a coordination model of a stochastic solar-wind-small hydropower system. In Ref. [29], the grey wolf algorithm (GWO) was hybridized with the analytic hierarchy process to perform a similar study on OPF. In [30], an adaptive FDB-based stochastic fractal search (AFDB-SFS) was suggested as a solution to address the OPF problem, which involves the integration of solar, wind, tidal, and small hydro energies. The authors in [31] developed a modified runge Kutta optimizer (MRUN) for handling stochastic OPF by incorporating a thyristor-controlled series compensator, wind turbine, and PV systems.

Several studies have investigated MOEAs for MOOPF problems with RESs. The non-dominated PSO (NSPSO) method was modified with stochastic weights and chaotic mutation in [32] to acquire non-dominated solutions while implementing a similar protocol for wind power, similar to that in [20]. The same framework was considered in [33] when using a multi-objective glowworm swarm optimizer (MOGWO). Stochastic modeling was formulated for small hydro, solar, and wind power uncertainties in [34] by applying summation-based multi-objective DE (SMODE) and MOEA/D to a power generation scheduling problem. In employing a constrained multi-objective population extremal optimizer (CMOPEO) in a multiobjective economic-emission framework, the authors in [35] considered the valve-point effects of thermal generators and costs for uncertain wind energy. In a recent study, the author demonstrated a multi-objective version of AGDE (MOAGDE) to solve the MOOPF problem, including solar, wind, and small hydropower sources replacing thermal generators at various nodes of a 30-node network [36]. Li et al. [37] adopted an adaptive crossover non-dominated sorting DE (ACNSDE) to resolve the MOOPF, wherein uncertain wind power was simulated using the Weibull probability density functions (PDF). The authors of [38] suggested an approach called the MOSGA to resolve the MOOPF problem with different PDFs for solar and wind energies. However, the valve-point effects of conventional generators were not investigated. Lv et al. [39] developed a multi-objective quadratic interpolation-learning DE (MOQILDE) to solve the MOOPF problem in hybrid power systems of thermal generators and solar photovoltaic plants. In [40], the MOOPF problem with stochastic tidal, solar, and wind energies was modeled and solved using a multi-objective pathfinder optimization algorithm (MOPFA). In that study, the authors investigated only a small-scale 30-bus system.

A brief comparison of the studies on MOOPF-RES problems is provided in Table 1. As deduced from the literature review and Table 1, the research gaps in MOOPF with stochastic RES penetration are as follows:

1. Although extensive research has been conducted on OPF incorporating RESs, MOOPF combined with RESs has been expressed as a single-objective framework of generation costs or as a multi-objective framework based on the weighted metric method [20–31]. The weighted metric method may not provide a suitable solution to multi-objective problems, particularly when the objective functions are conflicting. An appropriate approach for multi-objective problems is to use MOEAs to find a set of non-dominated solutions, thereby selecting an optimal solution

based on the preferences of the decision maker. However, a few studies have been conducted on MOOPF-RESs using MOEAs [32–40]. Among the applications of MOEAs, only two studies [37] and [40] investigated MOOPF-RESs problems with more than three-objective functions owing to their complexity. However, they used only a small-scale 30-bus network. Thus, MOOPF problems with RES should be further encouraged because of their importance in the context of the greater penetration of RES in modern power grids.

2. In multi-objective problems, the main goal of MOEAs is to generate a non-dominated set with good convergence and diversity. To achieve this goal, determining the geometry of the Pareto front is extremely important. The MOEAs used for MOOPF-RES problems in the literature were developed by implicitly assuming that the optimal front has a Euclidean geometry. However, the optimal front in multi-objective problems can be formed from a Euclidean, spherical, or hyperbolic hypersurface. This may have affected the diversity and convergence of the obtained solutions. Moreover, an increasing number of objectives significantly increases the complexity of the problem and requires more calculation time to define the optimal front. Therefore, a new robust method should be proposed to efficiently address MOOPF problems that incorporate RES.

3. Most published papers only studied MOOPF with RES on an adapted IEEE 30-bus network. The expansion of the problem to larger benchmark power grids has not yet been fully considered. This encourages studies to implement the MOOPF problem with RES to evaluate the effects of stochastic RESs on the optimal operational solutions for large-scale power systems.

This study aims to circumvent these problems and fill these gaps by developing a new adaptive geometry-estimation-based multi-objective differential evolution (AGE-MODE) method, which is suitable for MOOPF in hybrid thermal-wind-solar power systems (MOOPF-TWS). The proposed algorithm is inspired by the method of estimating the shape of a generated front using an adaptive geometry estimation (AGE) approach [41]. Therefore, AGE-MODE can significantly enhance the convergence and diversity of the generated Pareto front, regardless of whether it generates a Euclidean, spherical, or hyperbolic hypersurface. The new method solves the MOOPF-TWS problem with four objectives: total generation costs, emissions, real power loss, and voltage deviation. The developed method is simulated on IEEE 30-bus and 57-bus networks with diverse optimization objectives. The other salient contributions of this study are as follows:

- The MOOPF-TWS is formulated as a constrained multi-objective optimization problem in hybrid power systems in which thermal, wind, and solar PV power plants are scheduled in a coordinated manner. Four different objective functions are considered from economic, environmental, and technical perspectives. Weibull and lognormal PDFs are proposed to manage the uncertainty and intermittent nature of wind speed and solar irradiance.
- A new AGE-MODE is developed based on the framework of normalization, AGE, survival score calculation, and genetic operation of the DE method. AGE-MODE aims to provide the optimum Pareto front and proper trade-off for contradictory objective functions.
- To evaluate the proposed AGE-MODE, various case studies with combinations of two, three, or four objectives are conducted on modified IEEE 30-bus and 57-bus systems connected to RES. Based on the comparisons, AGE-MODE outperforms the other algorithms in terms of the optimal solution and values of performance metrics in most case studies.

The generation costs associated with thermal, wind, and solar sources are introduced in Section 2. The MOOPF-TWS problem is presented in Section 3. Section 4 presents the concepts of the proposed AGE-MODE and its application to the MOOPF-TWS. The simulation results are

outlined in Section 5, followed by conclusions in Section 6.

2. Mathematical models for generation costs

2.1. Thermal power

Thermal generators are operated using fossil fuels. The fuel cost is defined based on a quadratic correlation with the generated power, as follows [42]:

$$C_{TP}(P_{TP}) = \sum_{k=1}^{N_{TP}} \left(a_k + b_k P_{TP,k} + c_k P_{TP,k}^2 \right) \tag{1}$$

where N_{TP} is the total number of thermal power units, and a_k, b_k, and c_k are the cost coefficients of the kth thermal power unit corresponding to the output power $P_{TP,k}$.

Considering valve-point effects is necessary to model the thermal generator cost function in a realistic and efficient manner. The valve-point effects can be determined as a sinusoidal function and added to the total generation costs of the thermal power units, as follows [42,43]:

$$C_{TP}(P_{TP}) = \sum_{k=1}^{N_{TP}} \left(a_k + b_k P_{TP,k} + c_k P_{TP,k}^2 + \left| d_k \times \sin\left(e_k \times \left(P_{TP,k}^{\min} - P_{TP,k} \right) \right) \right| \right) \tag{2}$$

where $P_{TP,k}^{\min}$ is the minimum output power associated with the kth thermal power unit, and d_k and e_k are the coefficients representing the valve-point effects.

2.2. Direct cost of wind and solar power

In this study, it is assumed that wind and solar power plants are operated by private companies. According to power contract agreements, the grid operator is responsible for paying for the wind power purchased from the wind farm operators [44].

The direct cost function for the wind power plant is modeled as follows [20,34]:

$$C_{w,i}(P_{ws,i}) = K_{Dw,i} P_{ws,i} \tag{3}$$

where $P_{ws,i}$ and $K_{Dw,i}$ are the scheduled power and direct cost coefficients of the ith wind power plant, respectively.

The direct cost function for the solar PV power plant can be determined using Eq. (4) [20,34]:

$$C_{s,j}(P_{ss,j}) = K_{Ds,j} P_{ss,j} \tag{4}$$

where $P_{ss,j}$ and $K_{Ds,j}$ are the scheduled power and direct cost coefficients of the jth solar PV power plant, respectively.

2.3. Cost of wind power uncertainty

In view of the intermittent and uncertain nature of wind power plants, a possibility exists that they will not be able to generate scheduled power. If the actual wind power supplied by the wind power plant is less than the scheduled power, grid operators require reserve power sources to continuously supply power to consumers. The reserve cost for a wind power shortage should be paid for the reserve-generating units, which can be defined as follows [20,34]:

$$C_{Rw,i}\left(P_{ws,i} - P_{wav,i} \right) = K_{Rw,i} \int_0^{P_{ws,i}} (P_{ws,i} - p_{w,i}) f_w(p_{w,i}) dp_{w,i} \tag{5}$$

where $K_{Rw,i}$, $P_{wav,i}$, and $f_w(p_{w,i})$ are the reserve cost coefficient, actual available power, and PDF pertaining to the ith wind power plant, respectively.

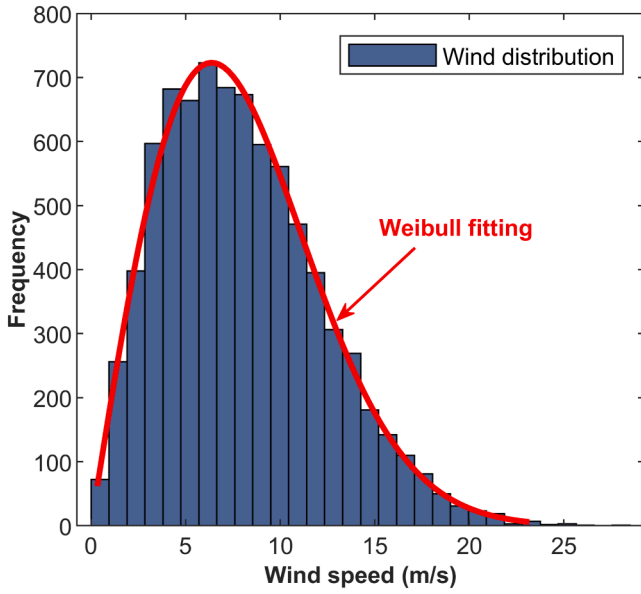If the wind power plant provides a larger amount of actual wind

Fig. 1. Wind speed distribution for a typical wind power plant ($\alpha = 9$, $\beta = 2$).

power than the scheduled power, the surplus power may be unused, and the grid operator is liable for the penalty cost. The penalty cost associated with the wind power surplus can be defined as follows [20,34]:

$$C_{Pw,i}\left(P_{wav,i} - P_{ws,i}\right) = K_{Pw,i} \int_{P_{ws,i}}^{P_{wr,i}} \left(p_{w,i} - P_{ws,i}\right) f_w\left(p_{w,i}\right) dp_{w,i} \tag{6}$$

where $K_{Pw,i}$ and $P_{wr,i}$ are the penalty cost coefficient and rated power of the ith wind power plant, respectively.

2.4. Cost of solar power uncertainty

Similar to wind power, the uncertain and intermittent power output of solar PV power plants also leads to overestimation and underestimation costs. The reserve cost of a solar PV power plant can be expressed in the following equation [20,34]:

$$C_{Rs,j}\left(P_{ss,j} - P_{sav,j}\right) = K_{Rs,j} \times f_s\left(P_{sav,j} < P_{ss,j}\right) \times \left[P_{ss,j} - E\left(P_{sav,j} < P_{ss,j}\right)\right] \tag{7}$$

where $K_{Rs,j}$ and $P_{sav,j}$ are the reserve cost coefficient and actual available power of the jth solar PV power plant, respectively; $E(P_{sav,j} < P_{ss,j})$ is the expectation of solar PV power lower than scheduled power ($P_{ss,j}$); and $f_s(P_{sav,j} < P_{ss,j})$ is the likelihood of shortfall of solar PV power.

The penalty cost associated with a solar PV power plant can be given by Eq. (8) [20,34]:

$$C_{Ps,j}\left(P_{sav,j} - P_{ss,j}\right) = K_{Ps,j} \times f_s\left(P_{sav,j} > P_{ss,j}\right) \times \left[E\left(P_{sav,j} > P_{ss,j}\right) - P_{ss,j}\right] \tag{8}$$

2.5. Stochastic wind and solar modeling

2.5.1. Uncertain wind power

The Weibull PDF can be applied to model wind speed distributions [20,45,46]. According to the Weibull PDF with a shape factor (β) and scale factor (α), the wind speed distribution can be modeled as follows [20,34]:

$$f_v(v) = \left(\frac{\beta}{\alpha}\right)\left(\frac{v}{\alpha}\right)^{(\beta-1)} e^{-(v/\alpha)^{\beta}}; \quad \text{for } 0 < v < \infty \tag{9}$$

where v is the wind speed (m/s).

Fig. 1 depicts the wind speed distribution for a typical wind power plant after running 8000 Monte-Carlo scenarios with the following Weibull parameters: $\alpha = 9$ and $\beta = 2$.

The actual available power related to the wind turbine can be formulated as follows [20,34]:

$$p_w(v) = \begin{cases} 0 & v < v_{in} \text{ and } v > v_{out} \\ p_{wr}\left(\dfrac{v - v_{in}}{v_r - v_{in}}\right) & v_{in} \leq v \leq v_r \\ p_{wr} & v_r < v \leq v_{out} \end{cases} \tag{10}$$

where p_{wr}, v_{in}, v_{out}, and v_r are the rated power, cut-in speed, cut-out speed, and rated speed of a turbine, respectively.

At certain wind speeds, the output power of the wind turbine is discrete, as indicated by Eq. (10). The wind power output is zero in the zones of wind speed (v) lower than the cut-in speed (v_{in}) and higher than the cut-out speed (v_{out}). The wind turbine reaches the rated power in the zone between the rated speed (v_r) and cut-out speed (v_{out}). The wind power probabilities in these discrete zones can be calculated using the following equations [20,34]:

$$f_w(p_w)\{p_w = 0\} = 1 - \exp\left[-\left(\frac{v_{in}}{\alpha}\right)^{\beta}\right] + \exp\left[-\left(\frac{v_{out}}{\alpha}\right)^{\beta}\right] \tag{11}$$

$$f_w(p_w)\{p_w = p_{wr}\} = \exp\left[-\left(\frac{v_r}{\alpha}\right)^{\beta}\right] - \exp\left[-\left(\frac{v_{out}}{\alpha}\right)^{\beta}\right] \tag{12}$$

In the zone between the cut-in speed (v_{in}) and rated speed (v_r), the power output of the wind turbine is continuous. For a continuous zone, the probability can be computed as follows [20,34]:

$$f_w(p_w) = \frac{\beta(v_r - v_{in})}{\alpha^{\beta} \times p_{wr}}\left[v_{in} + \frac{p_w}{p_{wr}}\left(v_r - v_{in}\right)\right]^{\beta-1} \exp\left[-\left(\frac{v_{in} + \frac{p_w}{p_{wr}}\left(v_r - v_{in}\right)}{\alpha}\right)^{\beta}\right] \tag{13}$$

Based on the probabilities for various wind speed zones, the right-hand side of the reserve cost in Eq. (5) can be expanded as follows [47]:

$$C_{Rw,i}\left(P_{ws,i} - P_{wav,i}\right) = K_{Rw,i} \int_0^{P_{ws,i}} \left\{ \left(P_{ws,i} - p_{w,i}\right) \frac{\beta(v_r - v_{in})}{\alpha^{\beta} \times P_{wr,i}}\left[v_{in} + \frac{p_{w,i}}{P_{wr,i}}\left(v_r - v_{in}\right)\right]^{\beta-1} \exp\left[-\left(\frac{v_{in} + \frac{p_{w,i}}{P_{wr,i}}\left(v_r - v_{in}\right)}{\alpha}\right)^{\beta}\right] \right\} dp_{w,i}$$
$$+ K_{Rw,i}\left(P_{ws,i} - 0\right) \times f_w\left(p_{w,i}\right)\{p_{w,i} = 0\} \tag{14}$$

where $K_{Ps,j}$ is the penalty cost coefficient of the jth solar PV power plant, $E(P_{sav,j} > P_{ss,j})$ is the expectation of solar PV power exceeding $P_{ss,j}$, and $f_s(P_{sav,j} > P_{ss,j})$ is the likelihood of an excess of solar PV power.

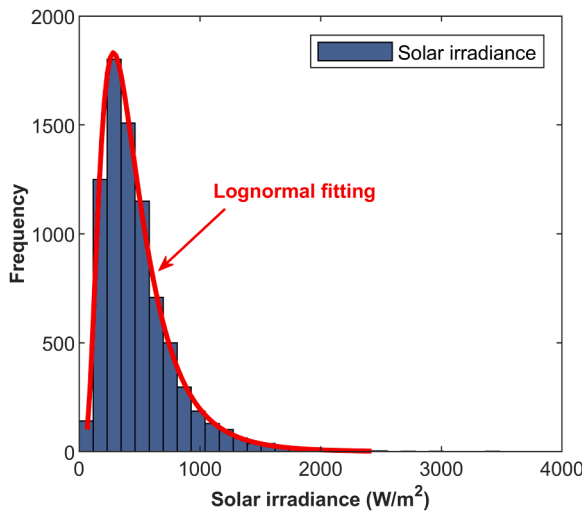Moreover, the right-hand side of the penalty cost in Eq. (6) can be expanded as follows [47]:

Fig. 2. Solar irradiation distribution for a typical solar PV ($\mu = 6$, $\sigma = 0.6$).

$$C_{Ps}\left(P_{sav} - P_{ss}\right) = K_{Ps} \sum_{n=1}^{N+} [P_{sn+} - P_{ss}] \times f_{sn+} \quad (20)$$

where P_{sn+} is the available power that is higher than the scheduled power, f_{sn+} is the proportionate occurrence frequency of P_{sn+}, and N^+ is the number of pairs (P_{sn+}, f_{sn+}) created for the PDF. For simplicity, the suffix 'j' in Eqs. (7) and (8) are not included to represent a single solar power plant.

3. Multi-objective optimal power flow of thermal-wind-solar power system (MOOPF-TWS)

In the MOOPF-TWS problem, the goal is to determine a set of control variables to optimize certain objective functions while satisfying the constraints related to equality and inequality [11,38]:

$$\text{Minimize} \quad f(u,x) = [f_1(u,x), f_2(u,x), \dots, f_M(u,x)] \quad (21)$$

$$s.t. \quad h(u,x) = 0 \quad (22)$$

$$C_{Pw,i}\left(P_{wav,i} - P_{ws,i}\right) = K_{Pw,i} \int_{P_{ws,i}}^{P_{wr,i}} \left\{ \left(\left(p_{w,i} - P_{ws,i}\right) \frac{\beta(v_r - v_{in})}{\alpha^\beta \times P_{wr,i}} \left[v_{in} + \frac{p_{w,i}}{P_{wr,i}}\left(v_r - v_{in}\right) \right]^{\beta-1} \exp\left[-\left(\frac{v_{in} + \frac{P_{w,i}}{P_{wr,i}}\left(v_r - v_{in}\right)}{\alpha} \right)^\beta \right] \right) \right\} dp_{w,i}$$
$$+ K_{Pw,i}\left(P_{wr,i} - P_{ws,i}\right) \times f_w\left(p_{w,i}\right)\{p_{w,i} = P_{wr,i}\} \quad (15)$$

2.5.2. Uncertain solar power

The solar irradiance distribution can be modeled correctly using a lognormal PDF [48]. Using the mean (μ) and standard deviation (σ) of the lognormal PDF, the probability of solar irradiance (G_s) can be expressed as follows [20,34]:

$$f_G(G_s) = \frac{1}{G_s \sigma \sqrt{2\pi}} \exp\left\{ \frac{-(\ln G_s - \mu)^2}{2\sigma^2} \right\}; \quad \text{for } G_s > 0 \quad (16)$$

Fig. 2 presents the solar irradiation distribution for a typical solar PV after running 8000 Monte-Carlo scenarios with the following lognormal parameters: $\mu = 6$ and $\sigma = 0.6$.

Energy conversion for solar PV is defined in the following equation [20,34]:

$$P_s(G_s) = \begin{cases} P_{sr}\left(\dfrac{G_s^2}{G_{std}R_c}\right) & \text{for } 0 < G_s < R_c \\ P_{sr}\left(\dfrac{G_s}{G_{std}}\right) & \text{for } G_s \geq R_c \end{cases} \quad (17)$$

where R_c is the irradiance point, G_{std} is the solar irradiance in a standard environment, and P_{sr} is the rated power of the solar PV.

The maximum penetration of solar PV into the system must be capped at the rated power of solar PV as follows [45]:

$$P_s \leq P_{sr} \quad (18)$$

The reserve cost in Eq. (7) can be expanded as follows [20,34]:

$$C_{Rs}\left(P_{ss} - P_{sav}\right) = K_{Rs} \sum_{n=1}^{N^-} [P_{ss} - P_{sn-}] \times f_{sn-} \quad (19)$$

where P_{sn-} is the available power that is lower than the scheduled power P_{ss}, f_{sn-} is the proportionate occurrence frequency of P_{sn-}, and N^- is the number of pairs (P_{sn-}, f_{sn-}) created for the PDF.

The penalty cost in Eq. (8) can be expanded as follows [20,34]:

$$g(u,x) \leq 0 \quad (23)$$

where f_M is the Mth objective; vector u is the control variables; vector x is the state variables; $h(u,x)$ and $g(u,x)$ are the sets of constraints for equality and inequality, respectively.

3.1. Objective function of optimization

3.1.1. Total generation costs

The total generation costs include the thermal power cost and the direct, penalty, and reserve costs involved in the wind and solar power sources, which can be expressed as follows [20]:

$$F_1 = C_{TP}(P_{TP}) + \sum_{i=1}^{N_{WP}} \left[C_{w,i}\left(P_{ws,i}\right) + C_{Rw,i}\left(P_{ws,i} - P_{wav,i}\right) + C_{Pw,i}\left(P_{wav,i} - P_{ws,i}\right) \right]$$
$$+ \sum_{j=1}^{N_{SP}} \left[C_{s,j}\left(P_{ss,j}\right) + C_{Rs,j}\left(P_{ss,j} - P_{sav,j}\right) + C_{Ps,j}\left(P_{sav,j} - P_{ss,j}\right) \right] \quad (24)$$

where N_{WP} and N_{SP} are the total numbers of wind and solar PV power plants, respectively.

3.1.2. Real power loss

Transmission systems inevitably suffer from power losses owing to the inherent resistance of the lines, which can be calculated as follows [4]:

$$F_2 = \sum_{n=1}^{N_L} G_{n(ij)} \left[V_i^2 + V_j^2 - 2V_i V_j \cos \delta_{ij} \right] \quad (25)$$

where $G_{n(ij)}$ is the transfer conductance of the nth branch connecting the ith bus and j^{th} bus; V_i and V_j are the voltage magnitudes at the ith bus and j^{th} bus, respectively; δ_{ij} is the difference in voltage angles between the ith bus and j^{th} bus; and N_L is the number of transmission lines.

3.1.3. Emissions

Power generated from thermal sources releases pollutants into the atmosphere. The overall emissions of harmful gases from fossil fuel thermal power plants are expressed as follows [42,49]:

$$F_3 = \sum_{k=1}^{N_{TP}} \left[\left(\alpha_k + \beta_k P_{TP,k} + \gamma_k P_{TP,k}^2 \right) + \omega_k e^{\left(\mu_k P_{TP,k} \right)} \right] \tag{26}$$

where α_k, β_k, γ_k, ω_k, and μ_k are coefficients of emission of the kth thermal power unit.

3.1.4. Voltage deviation

As an indicator of voltage quality in power systems, voltage deviation can be calculated as follows [4,43]:

$$F_4 = \sum_{i=1}^{N_D} |V_{L,i} - 1| \tag{27}$$

where $V_{L,i}$ is the voltage magnitude at the ith load bus, and N_D is the number of load buses.

3.2. Control variables

The vector u containing control variables is listed as follows:

$$u = \left[P_{TP,2}, \ldots, P_{TP,N_{TP}}, P_{ws,1}, \ldots, P_{ws,N_{WP}}, P_{ss,1}, \ldots, P_{ss,N_{SP}}, \ V_{G,1}, \ldots, V_{G,N_G}, T_1, \ldots, T_{N_T}, Q_{C,1}, \ldots, Q_{C,N_C} \right]^T \tag{28}$$

where P_{TP} is the real power generation of the thermal power unit, except for the reference bus; P_{ws} is the real power generation of the wind power plant; P_{ss} is the real power generation of the solar PV power plant; V_G is the generation bus voltage magnitude; T is the tap setting of the transformer; Q_C is the shunt VAR compensation; N_G, N_T, and N_C are the number of generation buses, the number of regulating transformers, and the number of VAR compensators, respectively.

3.3. State variables

The vector x comprising state variables can be listed as follows:

$$x = \left[P_{TP,1}, Q_{G,1}, \ldots, Q_{G,N_G}, S_{L,1}, \ldots, S_{L,N_L}, V_{L,1}, \ldots, V_{L,N_D} \right]^T \tag{29}$$

where $P_{TP,1}$ is the real power generation of the reference bus, Q_G is the reactive power generation of the generation buses, S_L is the transmission line loading, and V_L is the load bus voltage magnitude.

3.4. Technical constraints

3.4.1. Equality constraints

The equality constraints are typically determined by functions that describe the real and reactive power balances at each bus using the following equations:

$$P_{G,i} - P_{D,i} - V_i \sum_{j=1}^{N_B} V_j \left[G_{ij} \cos\left(\delta_{ij}\right) + B_{ij} \sin\left(\delta_{ij}\right) \right] = 0; \quad i = 1, ., N_B \tag{30}$$

$$Q_{G,i} - Q_{D,i} - V_i \sum_{j=1}^{N_B} V_j \left[G_{ij} \sin\left(\delta_{ij}\right) - B_{ij} \cos\left(\delta_{ij}\right) \right] = 0; i = 1, ., N_B \tag{31}$$

where N_B is the total number of buses; G_{ij} and B_{ij} are the transfer conductance and susceptance between the ith bus and j^{th} bus, respectively; $P_{G,i}$ and $Q_{G,i}$ are the real and reactive power generations from
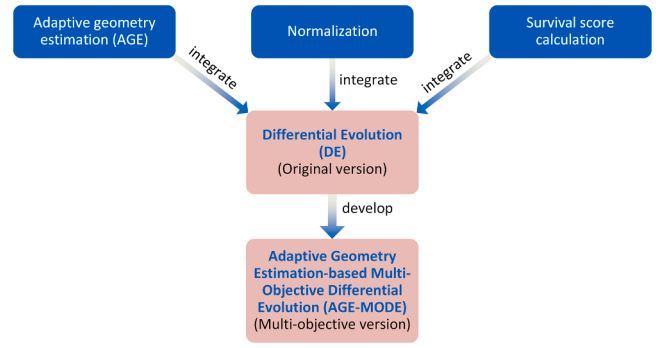
Fig. 3. Overall framework of the AGE-MODE algorithm.

power sources (thermal, wind, and solar), respectively. The real and reactive power demands at the ith load bus are denoted by $P_{D,i}$ and $Q_{D,i}$, respectively.

3.4.2. Inequality constraints

3.4.2.1. Generator constraints.
The real and reactive powers of the thermal, wind, and solar PV power plants, and generation bus voltage magnitudes must be bound by the lower and upper limits, as follows:

$$P_{TP,i}^{\min} \leq P_{TP,i} \leq P_{TP,i}^{\max}; \quad i = 1, ., N_{TP} \tag{32}$$

$$P_{ws,i}^{\min} \leq P_{ws,i} \leq P_{ws,i}^{\max}; \quad i = 1, ., N_{WP} \tag{33}$$

$$P_{ss,i}^{\min} \leq P_{ss,i} \leq P_{ss,i}^{\max}; \quad i = 1, ., N_{SP} \tag{34}$$

$$Q_{G,i}^{\min} \leq Q_{G,i} \leq Q_{G,i}^{\max}; \quad i = 1, ., N_G \tag{35}$$

$$V_{G,i}^{\min} \leq V_{G,i} \leq V_{G,i}^{\max}; \quad i = 1, ., N_G \tag{36}$$

3.4.2.2. Transformer constraints.
The tap settings of the transformers must be within lower and upper limits, as follows:

$$T_i^{\min} \leq T_i \leq T_i^{\max}; \quad i = 1, ., N_T \tag{37}$$

3.4.2.3. Shunt VAR compensator constraints.
The shunt compensators must be limited to the following lower and upper boundaries:

$$Q_{C,i}^{\min} \leq Q_{C,i} \leq Q_{C,i}^{\max}; \quad i = 1, ., N_C \tag{38}$$

3.4.2.4. Security constraints.
The complex power flow in transmission lines and load bus voltage magnitudes should be satisfied by physical limitations, as follows:

$$S_{L,i} \leq S_{L,i}^{\max}; \quad i = 1, ., N_L \tag{39}$$

$$V_{L,i}^{\min} \leq V_{L,i} \leq V_{L,i}^{\max}; \quad i = 1, ., N_D \tag{40}$$

4. AGE-MODE

In a multi-objective optimization problem, the main goal of MOEAs is to generate a set of non-dominated solutions that approximate the optimal Pareto front. The generated set of solutions should converge

well and diversify over the optimal front. The convergence and diversity significantly depend on the shape of the Pareto front which can be formed from a Euclidean, spherical, or hyperbolic hypersurface [41]. Precise estimation of the Pareto front shape can improve the performance of an algorithm in solving multi-objective problems. To this end, a new and effective multi-objective method called AGE-MODE is developed in this study by integrating the genetic operation of the DE algorithm with several frameworks, including normalization, AGE, and survival score calculation. The AGE approach [41] is used to estimate the geometry of the optimal front. Using the estimated geometry, a set of solutions is selected for the next generation based on their convergence and diversity using the survival score. The overall framework of AGE-MODE is shown in Fig. 3. Brief descriptions of the DE algorithm and the proposed AGE-MODE algorithm are provided in the following sections.

4.1. Differential evolution (DE)

DE is one of the most popular population-based optimization algorithms [50]. The control parameters that affect the DE performance include the population size, scale factor for the mutation strategy, and crossover rate for the crossover strategy. After initialization, the DE algorithm iteratively performs the mutation, crossover, and selection steps.

4.1.1. Initialization
DE initializes a population of candidate solutions with randomly assigned values, as follows:

$$x_{i,j}^{(0)} = x_j^{\min} + rand_{i,j}\left[0,1\right]\left(x_j^{\max} - x_j^{\min}\right); \quad i = 1, 2, ..., N_P, j = 1, 2, ..., D \tag{41}$$

where $x_{i,j}^{(0)}$ is the jth component of the ith solution vector of the population at initialization; $x_j^{\min}$ and $x_j^{\max}$ are the lower and upper bounds of the jth dimension of the search space, respectively; $rand_{i,j}[0,1]$ is a uniform random variable ranging from zero to one; D is the dimension of the solution vector; and N_P is the population size.

4.1.2. Mutation
At each Gth generation, DE performs mutations by creating a mutant vector for each population member as follows [50]:

$$v_i^{(G)} = x_{r1}^{(G)} + F \cdot \left(x_{r2}^{(G)} - x_{r3}^{(G)}\right) \tag{42}$$

where indices r_1, r_2, and r_3 are mutually exclusive integers chosen randomly from the population range, and a positive mutation factor (F) is used to regulate the amplitude of the differential variation.

4.1.3. Crossover
During the crossover, the trial vector $u_i^{(G)} = (u_{i,1}^{(G)}, u_{i,2}^{(G)}, ..., u_{i,D}^{(G)})$ is generated by mixing the elements of the mutant vector $v_i^{(G)}$ with the target vector $x_i^{(G)}$ to increase the diversity of the perturbed parameter vectors. This scheme is based on a binomial crossover and applies to each variable via an adapted crossover rate, as follows [50]:

$$u_{i,j}^{(G)} = \begin{cases} v_{i,j}^{(G)} & \text{if } j = j_{rand} \text{ or } rand_{i,j}[0,1] \le CR_i^{(G)} \\ x_{i,j}^{(G)} & \text{otherwise} \end{cases} \tag{43}$$

where j_{rand} is an integer selected at random from one to D, and CR is the crossover rate.

The value of CR is adaptively changed over iterations, as follows [50]:

$$CR^{(G)} = e^{-\frac{G}{G_{\max}}} \tag{44}$$

where $G_{\max}$ is the maximum number of iterations.

4.1.4. Selection
The objective values of the trial vectors are computed and compared with those of the target vectors. Trial vectors with better objective values replace the target vectors in the population. Selection is performed as follows [50]:

$$x_i^{(G+1)} = \begin{cases} u_i^{(G)} & \text{if } f\left(u_i^{(G)}\right) < f\left(x_i^{(G)}\right) \\ x_i^{(G)} & \text{otherwise} \end{cases} \tag{45}$$

where f is the objective function.

4.2. Normalization

In this study, fast non-dominated sorting of NSGA-II [51] is used to group a population into subsequent non-dominated fronts. Based on the normalization strategy of NSGA-III, the objective functions of the solution in the first non-dominated front ($\mathbf{F}_1$) can be normalized as follows [52,53]:

$$f_i^n(S) = \frac{f'_i(S)}{a_i} = \frac{f_i(S) - z_i^{\min}}{a_i}; \quad \forall S \in \mathbf{F}_1, i = 1, 2, ..., M \tag{46}$$

where M is the number of objectives, $f_i(S)$ is the ith objective function of solution S, and $z_i^{\min}$ is the minimum value of the ith objective function for all solutions in $\mathbf{F}_1$. The numerator denotes the transformed objective by subtracting each objective f_i using $z_i^{\min}$, enabling the ideal point to be equal to the origin of the axes. The term a_i denotes the intercept of the objective axis f_i with an M-dimensional hyperplane [52,53].

Based on the values of $z_i^{\min}$ and a_i computed for the first front, the solutions in all other fronts $\mathbf{F}_k$ (with $k > 1$) can be normalized. However, the normalized objectives for front $\mathbf{F}_1$ have values between zero and one, those for the other fronts may have values exceeding one.

4.3. Adaptive geometry estimation (AGE)

Generally, the norm of a vector $v = (v_1, ..., v_M)$ can be defined using L_p norm (or p-norm) in the M-dimensional space $\mathbf{R}^M$ as follows [54]:

$$\|v\|_p = (v_1^p + ... + v_M^p)^{1/p} \tag{47}$$

The distance measurements between points A_1 and A_2 in $\mathbf{R}^M$ differ based on the different values of p. The shape of the unit hypersurface related to the L_p norm is determined by the value of p [54]. To this end, an effective process called AGE is proposed for defining the shape of the non-dominated front [41].

In the proposed AGE, the central point in front $\mathbf{F}_1$ can be used to approximate the value of p. Therefore, the corresponding L_p exponential equation can be estimated precisely. In the normalized objective space, the central point C represents the point with the smallest perpendicular distance to the vector $\overrightarrow{\beta}$, which can be expressed as follows [41]:

$$C = \arg\min_{f^n(S)} dist^\perp\left(f^n(S), \overrightarrow{\beta}\right); \quad \forall S \in \mathbf{F}_1 \tag{48}$$

where the vector $\overrightarrow{\beta}$ is bounded by the ideal point ($Z^{\min} = (\overrightarrow{0})$) and the nadir point ($Z^{\max} = (\overrightarrow{1})$).

The value of the exponent p can be approximated as follows [41]:

$$p = \frac{\log(M)}{\log(M) - \log\left(\sum\limits_{i=1}^{M} C_i\right)} \tag{49}$$

where C_i is the ith coordinate of the central point C in the normalized objective space.

4.4. Survival score

The convergence and diversity of the first front $\mathbf{F}_1$ can be calculated by employing the geometry (L_p norm) of front $\mathbf{F}_1$ (defined in Section 4.3). For each non-dominated solution S, the convergence score can be defined as the distance between its objective vector and the ideal point based on the L_p norm, which can be expressed as follows [41]:

$$convergence(S) = \left\| f^n(S) - Z^{\min} \right\|_p = \left\| f^n(S) \right\|_p \tag{50}$$

From Eq. (50), a solution S with $convergence(S) < 1$ prevails in the parts of the unit hypersurface involved in the computed L_p norm. By contrast, solution S with $convergence(S) > 1$ is located farther distant from the ideal point than the other points in the unit hypersurface involved in L_p. The solution S with $convergence(S) = 1$ is located on the unit hypersurface of L_p.

values. After normalization, the solutions on all fronts are assigned their corresponding survival scores, which include convergence and diversity scores based on the L_p norm. In each generation, the exponent p of the L_p norm is approximated based on the geometry of the first front, as presented in Section 4.3. Therefore, the L_p norm can be adapted iteratively. Thus, the geometric estimation (i.e., the estimated value of p) of the Pareto front is more accurate if the first front is closer to the optimal front. Finally, a new population (with size N_p) is selected for the next generation, wherein the solutions in the first front ($\mathbf{F}_1$) are chosen first. The selection continues with the next fronts ($\mathbf{F}_2$, $\mathbf{F}_3$, …, $\mathbf{F}_k$) until the new population contains N_p solutions. For the last front ($\mathbf{F}_k$) to which its solutions can be added, the remaining solutions from $\mathbf{F}_k$ are selected in descending order of survival scores. The algorithm loop is executed until the stop criterion is satisfied.

Algorithm 1. AGE-MODE.

```
Input: M: Number of objectives
       N_P: Population size
Result: Final population P
begin
    P ← RANDOM-POPULATION(N_P)
    while not (stop_condition) do
        Q ← GENERATE-OFFSPRING(P)
        F ← FAST-NONDOMINATED-SORTING(P ⋃ Q)
        F ← NORMALIZE(F)
        p ← GET-GEOMETRY(F_1, M)              /* Eq.(49) */
        k ← 1                        /* First non-dominated rank */
        while |P| + |F_k| ⩽ N do
            SURVIVAL-SCORE(F_k, k, p)
            P ← P ⋃ F_k
            k ← k + 1
        SORT(F_k)                    /* based on survival scores */
        P ← P ⋃ F_k[1 : (N − |P|)]
    return P
```

For solutions $S \in \mathbf{F}_1$, the diversity score can be calculated as the minimum distance of S from all other solutions in $\mathbf{F}_1$ using the estimated p-norm [41]:

$$diversity\left(S, \mathbf{F}_1 \right) = \min_{T \neq S \in \mathbf{F}_1} \left\| f^n(S) - f(T) \right\|_p \tag{51}$$

With defined convergence and diversity scores, the survival score of each solution $S \in \mathbf{F}_1$ is determined by the following equation [41]:

$$score(S) = \frac{diversity(S, \mathbf{F}_1)}{convergence(S)} \tag{52}$$

4.5. Proposed AGE-MODE

The proposed AGE-MODE method is outlined in Algorithm 1. The optimization process begins by randomly creating an initial population P with N_p solutions in the search space. New solutions for the offspring population Q are created based on the genetic operation of the DE algorithm. A new population R with size $2 \times N_p$ is formed by combining the current population P and offspring population Q. Population R is then sorted into several non-dominated fronts ($\mathbf{F}_1$, $\mathbf{F}_2$, …, $\mathbf{F}_k$) using fast non-dominated sorting. In the following step, a procedure similar to that in NSGA-III is used to normalize all fronts by scaling the objective

4.6. Application of the AGE-MODE for the MOOPF-TWS problem

The application procedures of the AGE-MODE for the MOOPF-TWS problem are presented in Fig. 4 and outlined as follows:

4.6.1. Input

(i) MOOPF-TWS problem under study (power system data, dimensions of the problem, boundaries for control variables, objective functions to be considered, and set of equality and inequality constraints); (ii) AGE-MODE parameters (population size N_P, maximum iterations $G_{\max}$, and mutation factor F).

4.6.2. Output

Final Pareto optimal set and compromise solution.

4.6.3. Initialization

Randomly initialize a population of N_P candidate solutions, as shown in Eq. (41). Perform power flow computation based on the Matpower toolbox [55] to compute the fitness function value for all candidate solutions in the initial population. The inequality constraints are imposed on a fitness function as quadratic penalty terms as follows:
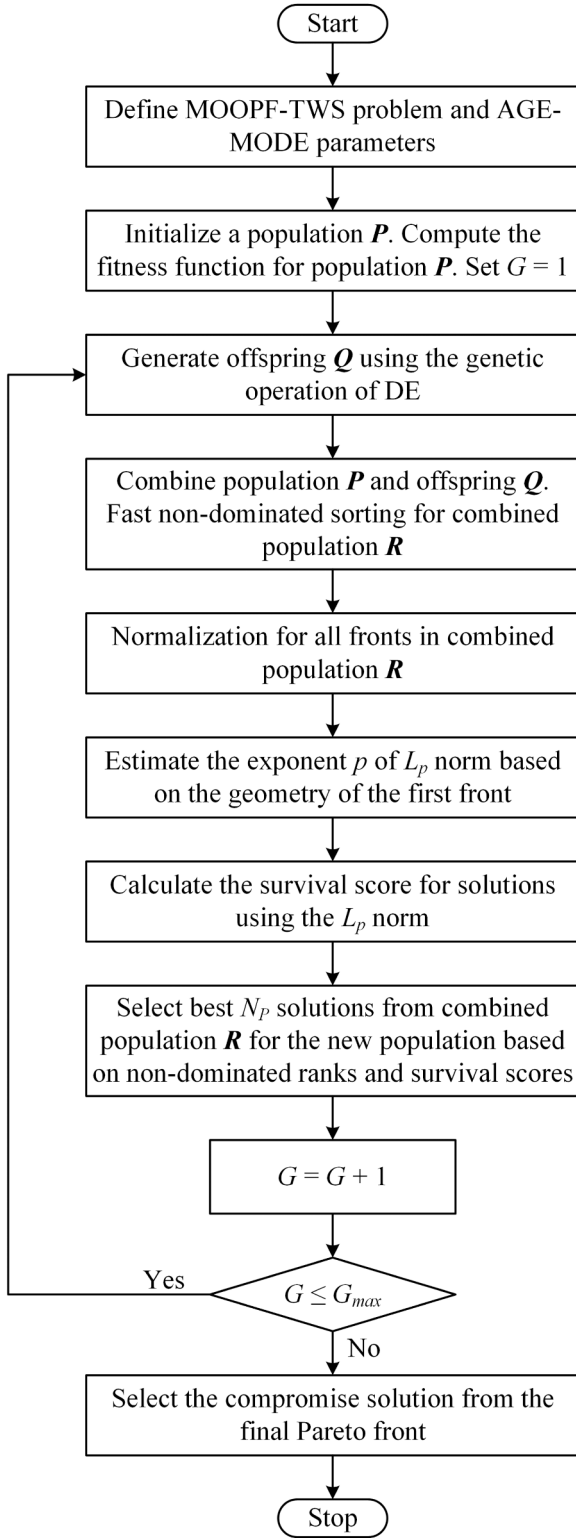
Fig. 4. Flowchart for implementation of AGE-MODE algorithm for the MOOPF-TWS problem.

$$FF_m = F_m + \lambda_P \left(P_{G,1} - P_{G,1}^{\lim} \right)^2 + \lambda_Q \sum_{k=1}^{N_G} \left(Q_{G,k} - Q_{G,k}^{\lim} \right)^2 + \lambda_S \sum_{k=1}^{N_L} \left(S_{L,k} - S_{L,k}^{\max} \right)^2$$
$$+ \lambda_V \sum_{k=1}^{N_D} \left(V_{L,k} - V_{L,k}^{\lim} \right)^2 \tag{53}$$

where λ_P, λ_Q, λ_S, and λ_V are penalty factors, F_m is the mth objective value, and $x^{\lim}$ is the limit value of the dependent variable x, which is obtained as follows:

$$x^{\lim} = \begin{cases} x_{\max}; & \text{if } x > x_{\max} \\ x_{\min}; & \text{if } x < x_{\min} \end{cases} \tag{54}$$

Algorithm loop:

Step 1: Set $G = 1$.

Step 2: Generate offspring population Q based on the genetic operation of the DE algorithm.

Step 3: Combine population P and offspring population Q into a combined population R. Group the combined population R into several non-dominated fronts ($\mathbf{F}_1$, $\mathbf{F}_2$, ..., $\mathbf{F}_k$) using the fast non-dominated sorting approach of NSGA-II.

Step 4: Apply the normalization approach of NSGA-III to normalize all fronts in the combined population R.

Step 5: Calculate the exponent p of the L_p norm on the geometry of the first front.

Step 6: Calculate the survival score using the predefined L_p norm for the solutions on all fronts.

Step 7: Select the best N_P solutions from the combined population R for the new population based on their non-dominated ranks and survival scores.

Step 8: Set $G = G + 1$. If $G \leq G_{\max}$, return to Step 2; otherwise, stop the algorithm.

Step 9: The compromise solution is selected from the Pareto optimal set based on a fuzzy decision-making approach. The membership function of an objective is computed as follows [56]:

$$\mu_{km} = \begin{cases} 1 & \text{if } F_{km} \leq \min(F_m) \\ \dfrac{\max(F_m) - F_{km}}{\max(F_m) - \min(F_m)} & \text{if } \min(F_m) \leq F_{km} \leq \max(F_m) \\ 0 & \text{if } F_{km} \geq \max(F_m) \end{cases} \tag{55}$$

where μ_{km} and F_{km} are the membership function and objective value of the mth objective for the kth solution, respectively; and $\max(F_m)$ and $\min(F_m)$ are the extreme values for the mth objective. The normalized membership function for the kth solution is determined using Eq. (56):

$$\mu_k = \frac{\sum_{m=1}^{M} \mu_{km}}{\sum_{k=1}^{N_d} \sum_{m=1}^{M} \mu_{km}} \tag{56}$$

where N_d is the number of Pareto optimal solutions. The solution with the highest μ_k value is defined as the compromise solution.

5. Simulation results

This study applies the proposed AGE-MODE method to resolve the MOOPF-TWS problem. Figs. 5 and 6 depict graphical diagrams of the modified IEEE 30-bus and 57-bus systems, respectively. For the modified IEEE 30-bus system shown in Fig. 5, three thermal power plants are located on buses 1, 2, and 8, two wind power plants are connected to buses 5 and 11, and one solar PV power plant is integrated at bus 13 [20]. As shown in Fig. 6, for the modified 57-bus system, four thermal power plants are located on buses 1, 3, 8, and 12, and two wind power plants are integrated into buses 6 and 9 along with a solar PV power plant on bus 2 [38]. The rated output power of the wind turbine is 3 MW. The other relevant system characteristics are referred from [57]. Appendix A provides the cost and emission coefficients associated with thermal power plants. The wind and solar outputs are the uncertainty variables, and the relevant parameters for modeling their respective uncertainties are listed in Tables 2 and 3. For an efficient and economical system operation, the MOOPF-TWS problem includes 24 control
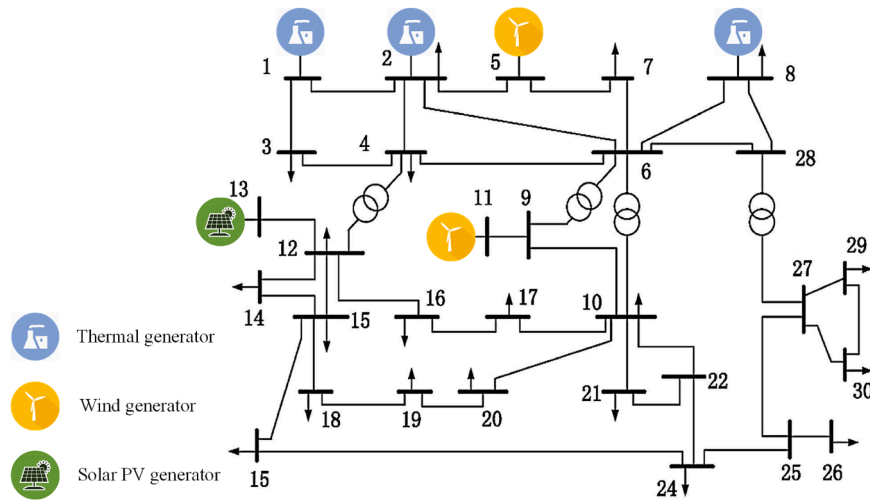
Fig. 5. IEEE 30-bus system connected to RES.

variables for a 30-bus system and 33 control variables for a 57-bus system, as defined in Eq. (28).

Different case studies are investigated for modified IEEE 30-bus and 57-bus systems. The details of each case study are presented in Table 4, wherein four objectives are considered in combination with two-, three-, or four-objective optimization problems. Cases 4 and 8 are considered the most challenging cases, in which all four-objective functions are optimized simultaneously.

All the simulations are performed using MATLAB 2020b. In this study, the AGE-MODE is performed with an adaptive crossover rate (in Eq. (44)) and a mutation probability of 0.5. Furthermore, the population size and maximum iterations of AGE-MODE related to each case study are referred from previous studies [11,34,37], as listed in Table 5. In addition, multi-objective differential evolution (MODE) and two recently developed multi-objective methods, namely, a knee-point-driven evolutionary algorithm (KnEA) [58] and reference
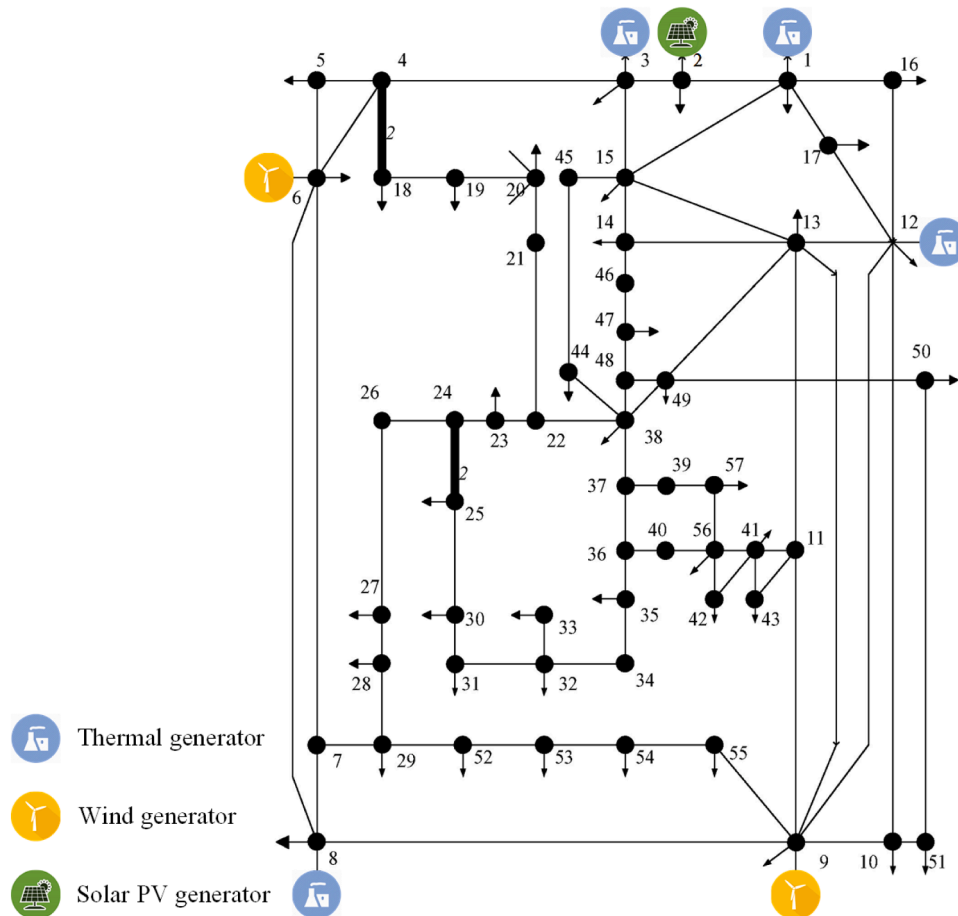
Fig. 6. IEEE 57-bus system connected to RES.

Table 2

IEEE 30-bus and 57-bus systems: PDF parameters and cost coefficients of wind power plant [20,34].

Items	IEEE 30-bus		IEEE 57-bus	
Number of wind turbines	25	20	50	40
Rated power (MW)	75 (bus 5)	60 (bus 11)	150 (bus 6)	120 (bus 9)
Direct cost coefficient ($/MW)	1.6	1.75	16	17.5
Reserve cost coefficient ($/MW)	3	3	30	30
Penalty cost coefficient ($/MW)	1.5	1.5	15	15
Weibull mean	$v = 7.976$ m/s	$v = 8.862$ m/s	$v = 7.976$ m/s	$v = 8.862$ m/s
Weibull PDF parameters	$\alpha = 9, \beta = 2$	$\alpha = 10, \beta = 2$	$\alpha = 9, \beta = 2$	$\alpha = 10, \beta = 2$

Table 3

IEEE 30-bus and 57-bus systems: PDF parameters and cost coefficients of solar PV power plant [20,34].

Items	IEEE 30-bus	IEEE 57-bus
Rated power (MW)	50 (bus 13)	80 (bus 2)
Direct cost coefficient ($/MW)	1.6	16
Reserve cost coefficient ($/MW)	3	30
Penalty cost coefficient ($/MW)	1.5	15
Lognormal mean	$G = 483$ W/m2	$G = 483$ W/m2
Lognormal PDF parameters	$\mu = 6, \sigma = 0.6$	$\mu = 6, \sigma = 0.6$

Table 4

Details of considered objective functions for each case study in the MOOPF-TWS problem.

Case	Generation costs	Emissions	Real power loss	Voltage deviation	System
Case 1	✔	✔			IEEE 30-bus system
Case 2	✔		✔		
Case 3	✔	✔	✔		
Case 4	✔	✔	✔	✔	
Case 5	✔	✔			IEEE 57-bus system
Case 6	✔		✔		
Case 7	✔	✔	✔		
Case 8	✔	✔	✔	✔	

Table 5

Parameter settings of AGE-MODE for solving MOOPF-TWS problem.

Parameters	Cases 1, 2, 3	Case 4	Cases 5, 6, 7	Case 8
Population size	100	200	100	200
Maximum iterations	300	600	500	1000

point dominance-based NSGA-II (RPD-NSGAII) [59], are reimplemented for similar problems with the same initial parameters to verify the performance of the proposed AGE-MODE. For each case, 30 Pareto fronts are qualitatively evaluated by estimating their hypervolume

Table 6

Simulation results for Cases 1, 2, 3, and 4.

Parameters	Min	Max	Case 1	Case 2	Case 3	Case 4
P_{TP2} (MW)	20	80	39.6562	20.9945	38.0771	37.8031
P_{ws1} (MW)	0	75	48.3428	59.2240	65.3183	68.1471
P_{TP3} (MW)	10	35	10	10.7693	22.7468	26.2153
P_{ws2} (MW)	0	60	40.3315	43.4286	46.4863	47.6580
P_{ss1} (MW)	0	50	40.2789	34.2933	40.7363	40.5389
V_{G1} (p.u.)	0.95	1.1	1.0652	1.0679	1.0649	1.0253
V_{G2} (p.u.)	0.95	1.1	1.0550	1.0537	1.0537	1.0145
V_{G5} (p.u.)	0.95	1.1	1.0362	1.0383	1.0415	1.0073
V_{G8} (p.u.)	0.95	1.1	1.0371	1.0386	1.0393	1.0024
V_{G11} (p.u.)	0.95	1.1	1.0587	1.0764	1.0809	1.0508
V_{G13} (p.u.)	0.95	1.1	1.0638	1.0528	1.0581	1.0043
T_{11} (p.u.)	0.9	1.1	1.0137	1.0663	1.0501	1.0601
T_{12} (p.u.)	0.9	1.1	0.9639	0.9	0.9319	0.9
T_{15} (p.u.)	0.9	1.1	0.9990	0.9905	0.9903	0.9636
T_{36} (p.u.)	0.9	1.1	0.9916	0.9742	0.9699	0.9651
Q_{C10} (MVar)	0	5	4.1690	1.7855	3.6306	1.9034
Q_{C12} (MVar)	0	5	0	5	0	2.4646
Q_{C15} (MVar)	0	5	5	1.6677	1.8866	2.1481
Q_{C17} (MVar)	0	5	3.7797	3.6482	3.2231	3.0304
Q_{C20} (MVar)	0	5	3.9551	4.6747	5	4.1995
Q_{C21} (MVar)	0	5	4.9725	5	4.9270	4.9986
Q_{C23} (MVar)	0	5	4.7945	4.0589	2.1824	5
Q_{C24} (MVar)	0	5	3.9419	5	4.8787	5
Q_{C29} (MVar)	0	5	2.9466	2.4799	0.9036	1.7534
Generation costs ($/h)	-	-	807.1515	803.9183	846.7070	854.6103
Emissions (ton/h)	-	-	0.4152	0.6930	0.1229	0.1105
Real power loss (MW)	-	-	4.5369	4.3028	2.7585	2.7106
Voltage deviation (p.u.)	-	-	0.7895	0.8955	0.8475	0.1315
P_{TP1} (MW)	50	200	109.3275	118.9931	72.7936	65.7483
Q_{G1} (MVar)	-20	150	-8.1422	-1.7503	3.4433	5.1880
Q_{G2} (MVar)	-20	60	11.8356	5.5076	-0.1329	0.3326
Q_{G5} (MVar)	-15	40	23.9276	22.4946	23.3406	28.1789
Q_{G8} (MVar)	-30	35	26.3197	27.3360	22.2785	28.3498
Q_{G11} (MVar)	-25	30	10.8836	23.2922	23.7823	26.7296
Q_{G13} (MVar)	-20	25	11.5628	2.8940	8.5120	-4.2672

values, and the best Pareto front has the highest hypervolume value.

The hypervolume metric is a well-established indicator for estimating the diversity and convergence of a generated Pareto front in multi-objective problems. This metric is estimated as follows [60]:

$$HV = \bigcup_{S=1}^{|\Omega|} v_S \tag{57}$$

where v_S is a hypercube for each solution $S \in \Omega$ created using a reference point [10].

To further validate the performance of the proposed algorithm, it is tested using the CEC2020 benchmark test functions. The comparative results between AGE-MODE and published results for the CEC2020 test problems are provided in Appendix B.

5.1. IEEE 30-bus system

For case studies related to the IEEE 30-bus system, Table 6 lists the optimum settings for all control variables, objective function values, and other related parameters for the compromise solutions. Tables 7 and 8 provide comparisons between the proposed AGE-MODE and other MOEAs in terms of the compromise solution associated with Cases 1–4. The load bus voltage profiles in Cases 1–4 are depicted in Fig. 7, which is an important factor for the optimal operation of the power system. As shown in Fig. 7, the constraints on the load bus voltages are fully satisfied in all cases. Considering the voltage deviation objective, the voltage configuration of Case 4 is better than that of the other cases. As shown in Figs. 8–10, the Pareto fronts generated by AGE-MODE for

Table 7

Comparisons of compromise solutions between AGE-MODE and other methods for Cases 1, 2, and 3.

Algorithm	Case 1		Case 2		Case 3		
	Costs ($/h)	Emissions (ton/h)	Costs ($/h)	Loss (MW)	Costs ($/h)	Emissions (ton/h)	Loss (MW)
AGE-MODE	807.1515	0.4152	**803.9183**	**4.3028**	846.7070	0.1229	**2.7585**
MODE	807.9098	0.4242	805.7954	4.3672	850.0573	0.1185	2.9021
KnEA	807.5084	0.4196	804.3478	4.3049	846.9837	0.1314	2.7751
RPD-NSGAII	807.3938	0.4809	806.2267	4.4052	861.2237	**0.0994**	2.7657
NSGAII-SF [37]	856.95	0.101	-	-	853.54	0.1181	2.8492
ACNSDE-SF [37]	843	0.123	-	-	**827.33**	0.1965	4.1918
SHADE-SF [20]	**792.516**	0.891	-	-	-	-	-

Table 8

Comparison of compromise solutions between AGE-MODE and other methods for Case 4.

Algorithm	Costs ($/h)	Emissions (ton/h)	Loss (MW)	Voltage deviation (p.u.)
AGE-MODE	854.6103	**0.1105**	**2.7106**	**0.1315**
MODE	854.1541	0.1342	3.0709	0.1387
KnEA	846.2292	0.1436	3.0912	0.1555
RPD-NSGAII	**810.7787**	0.4796	4.3518	0.2360
NSGAII-SF [37]	845.32	0.4279	4.2069	0.3979
ACNSDE-SF [37]	837.46	0.1804	3.6984	0.4179

Cases 1–3 are the best ones with the best hypervolume values over 30 runs in each case. It can be inferred from Figs. 8–10 that AGE-MODE can find Pareto fronts with high diversity that are also well distributed. For Case 4, the best Pareto front is shown as a parallel coordinate plot in Fig. 11. To this end, the values of the four objectives are normalized. According to Fig. 11, the non-dominated solutions found by AGE-MODE are distributed properly in the simultaneous optimization of the four-objective functions.

In Case 1 of generation costs and emissions optimization, AGE-MODE obtains a compromise solution with 807.1515 $/h of generation costs and 0.4152 ton/h of emissions, which shows considerable superiority over the MODE, KnEA, and RPD-NSGAII in terms of compromise solution. Moreover, AGE-MODE has a better generation cost value than NSGA-II-SF [37] and ACNSDE-SF [37] methods in published studies, wherein NSGAII-SF [37] and ACNSDE-SF [37] obtain the lowest emission values but with significantly high generation costs. By contrast, SHADE-SF [20] obtains the lowest cost value with an extremely high
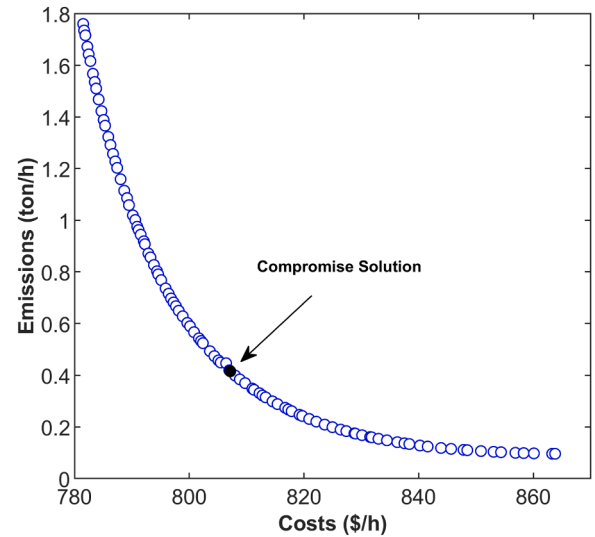
Fig. 8. Pareto front yielded by AGE-MODE for Case 1.

emission value. SHADE-SF [20] uses the weighted metric method to convert a multi-objective function of costs and emissions into a single-objective function which may make its solution biased toward cost minimization. The compromise solution of AGE-MODE is selected based on the distribution of non-dominated solutions along the Pareto front. As shown in Fig. 8, the Pareto front generated by AGE-MODE has a uniform distribution. Therefore, AGE-MODE can effectively choose a better compromise solution for both cost and emission objectives.
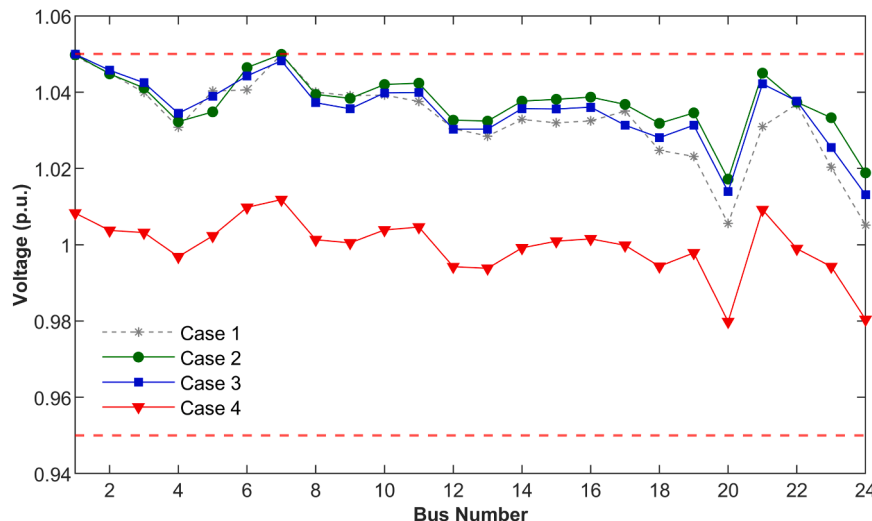
Fig. 7. Load bus voltage profiles for compromise solutions for Cases 1–4.

Fig. 9. Pareto front yielded by AGE-MODE for Case 2.

Fig. 10. Pareto front yielded by AGE-MODE for Case 3.

Fig. 11. Parallel coordinates plot for Pareto front yielded by AGE-MODE for Case 4.

Because of the simultaneous optimization of generation costs and power loss, the compromise solution achieved from AGE-MODE is 803.9183 $/h and 4.3028 MW in Case 2. Thus, the AGE-MODE solution outperforms MODE (805.7954 $/h and 4.3672 MW), KnEA (804.3478 $/h and 4.3049 MW), and RPD-NSGAII (806.2267 $/h and 4.4052 MW).

A few studies have been conducted on the MOOPF-TWS with more than two objectives. In this regard, this study considers three- and four-objective functions for the MOOPF-TWS problem in Cases 3 and 4, respectively. For Case 3 with three-objective functions, AGE-MODE can dominate KnEA over all three-objective values, as listed in Table 7. Moreover, AGE-MODE achieves lower generation costs and power loss than MODE and RPD-NSGAII. Compared to the published results, AGE-MODE is better than NSGAII-SF [37] and ACNSDE-SF [37] in terms of two of the three objectives. When four objectives are considered (Case 4), the compromise solution of AGE-MODE outperforms MODE, KnEA, RPD-NSGAII, NSGAII-SF [37], and ACNSDE-SF [37] for three of the four objectives, as shown in Table 8. Specifically, the values of emission, power loss, and voltage deviation obtained by AGE-MODE are the lowest in this case. Consequently, AGE-MODE can achieve the most advantageous solutions for Cases 1–4.

5.2. IEEE 57-bus system

The literature on the extension of the MOOPF-TWS problem to a 57-bus IEEE system is extremely limited. For Cases 5–8 related to the IEEE 57-bus network, the optimal settings of the control variables, objective function values, and other related parameters for the compromise solutions are listed in Table 9. Fig. 12 depicts voltage profiles for all cases with a permissible range [0.94 p.u.–1.06 p.u.]. In all cases, AGE-MODE finds solutions that validly satisfy the system constraints, including the reactive power outputs and load bus voltage, as expressed in the data obtained in Table 9 and Fig. 12. The best Pareto fronts generated by the proposed AGE-MODE are shown in Figs. 13–15. Figs. 13–15 show that AGE-MODE can obtain solutions that distribute fairly well and uniformly spread over the entire Pareto optimal region. As shown in Fig. 16, the parallel coordinate plot for Case 8 shows a reasonable distribution of the non-dominated solutions.

Comparisons of the compromise solutions between the proposed AGE-MODE and other MOEAs associated with Cases 5–8 are listed in Tables 10–11. In Case 5, the compromise solution obtained by AGE-MODE provides generation costs of 39569.94 $/h and emissions of 1.0552 ton/h, which is better than MODE (39611.65 $/h and 1.0773 ton/h) and KnEA (39583.73 $/h and 1.0593 ton/h). Furthermore, AGE-MODE achieves lower emissions at a higher generation cost than RPD-NSGA. Similarly, with a compromise solution of 39390.05 $/h and 10.9636 MW in Case 6, AGE-MODE dominates MODE and KnEA in terms of generation costs and power loss.

In the three-objective optimization in Case 7, AGE-MODE dominates all others on all objective functions. In addition, the solution of AGE-MODE is 40148.14 $/h, 1.0572 ton/h, and 11.0907 MW, which is considerably lower than those of MODE (40227.87 $/h, 1.1439 ton/h, and 11.8509 MW), KnEA (40220.11$/h, 1.0669 ton/h, and 11.2597 MW), and RPD-NSGAII (40982.58$/h, 1.0706 ton/h, and 12.5566 MW). In Case 8, with four-objective optimization, the solution yielded by AGE-MODE outperforms the solution yielded by MODE and RPD-NSGAII in all four objectives, and the solution yielded by KnEA in three of the four objectives. These comparisons show that the developed AGE-MODE has better convergence and diversity abilities than other approaches. The superior performance of AGE-MODE is more evident in complex cases with three- and four-objective optimizations.

5.3. Hypervolume metric analysis

In this section, the developed AGE-MODE is compared with other methods in terms of a hypervolume metric to comprehensively evaluate its effectiveness. The hypervolume metric is a robust indicator for

Table 9
Simulation results for Cases 5, 6, 7, and 8.

| Parameters	Min	Max	Case 5	Case 6	Case 7	Case 8
P_{ss1} (MW)	0	80	80	75.2123	78.8544	79.8137
P_{TP2} (MW)	40	140	68.9986	53.6034	83.6241	70.2698
P_{ws1} (MW)	0	150	150	110.0286	147.4609	149.8842
P_{TP3} (MW)	100	550	348.7883	352.2710	293.0464	294.8708
P_{ws2} (MW)	0	120	120	112.4568	119.8788	120
P_{TP4} (MW)	100	410	330.1518	410	389.6982	398.8717
V_{G1} (p.u.)	0.95	1.1	1.0568	1.0573	1.0532	1.0182
V_{G2} (p.u.)	0.95	1.1	1.0533	1.0519	1.0482	1.0100
V_{G3} (p.u.)	0.95	1.1	1.0542	1.0494	1.0474	1.0081
V_{G6} (p.u.)	0.95	1.1	1.0627	1.0564	1.0618	0.9993
V_{G8} (p.u.)	0.95	1.1	1.0634	1.0617	1.0604	1.0167
V_{G9} (p.u.)	0.95	1.1	1.0474	1.0484	1.0477	1.0121
V_{G12} (p.u.)	0.95	1.1	1.0425	1.0439	1.0458	1.0198
T_{19} (p.u.)	0.9	1.1	1.0183	0.9708	1.0046	0.9814
T_{20} (p.u.)	0.9	1.1	1.0337	1.0188	1.0432	1.0646
T_{31} (p.u.)	0.9	1.1	1.0774	1.0015	1.0351	0.9696
T_{35} (p.u.)	0.9	1.1	0.9938	0.9446	1.0814	1.0445
T_{36} (p.u.)	0.9	1.1	1.0232	1.0417	0.9	1.0895
T_{37} (p.u.)	0.9	1.1	1.0276	1.0270	0.9991	0.9942
T_{41} (p.u.)	0.9	1.1	0.9963	0.9941	0.9973	0.9869
T_{46} (p.u.)	0.9	1.1	0.9580	0.9419	0.9287	0.9176
T_{54} (p.u.)	0.9	1.1	0.9172	0.9089	0.9718	0.9
T_{58} (p.u.)	0.9	1.1	0.9767	0.9715	0.9817	0.9431
T_{59} (p.u.)	0.9	1.1	0.9682	0.9654	0.9871	0.9571
T_{65} (p.u.)	0.9	1.1	0.9972	0.9809	1.0116	1.0038
T_{66} (p.u.)	0.9	1.1	0.9460	0.9388	0.9592	0.9
T_{71} (p.u.)	0.9	1.1	0.9894	0.9757	0.9830	0.9584
T_{73} (p.u.)	0.9	1.1	0.9810	0.9862	1.0444	0.9936
T_{76} (p.u.)	0.9	1.1	0.9767	0.9678	0.9223	0.9091
T_{80} (p.u.)	0.9	1.1	1.0093	0.9866	0.9998	0.9786
Q_{C18} (MVar)	0	20	7.0316	9.0650	5.7046	18.4230
Q_{C25} (MVar)	0	20	12.5325	10.9718	12.9038	20
Q_{C53} (MVar)	0	20	11.8358	12.6392	14.2415	19.2856
Generation costs ($/h)	-	-	39569.94	39390.05	40148.14	40001.76
Emissions (ton/h)	-	-	1.0552	1.3008	1.0572	1.0925
Real power loss (MW)	-	-	13.8468	10.9636	11.0907	12.4100
Voltage deviation (p.u.)	-	-	1.3010	1.5075	1.2339	0.6543
P_{TP1} (MW)	0	576	166.7080	148.1916	149.3278	149.4998
Q_{G1} (MVar)	-140	200	42.6725	52.0374	46.1247	53.7541
Q_{G2} (MVar)	-30	40	38.3238	36.5571	35.2782	26.3478
Q_{G3} (MVar)	-10	60	44.4934	35.0535	26.1958	35.2576
Q_{G6} (MVar)	-60	75	-2.1373	-2.3417	6.3088	-44.2756
Q_{G8} (MVar)	-140	200	29.2202	26.7066	26.4027	25.0813
Q_{G9} (MVar)	-50	60	29.3442	38.6980	33.2786	42.4549
Q_{G12} (MVar)	-150	155	55.7605	37.9556	53.4254	79.3861
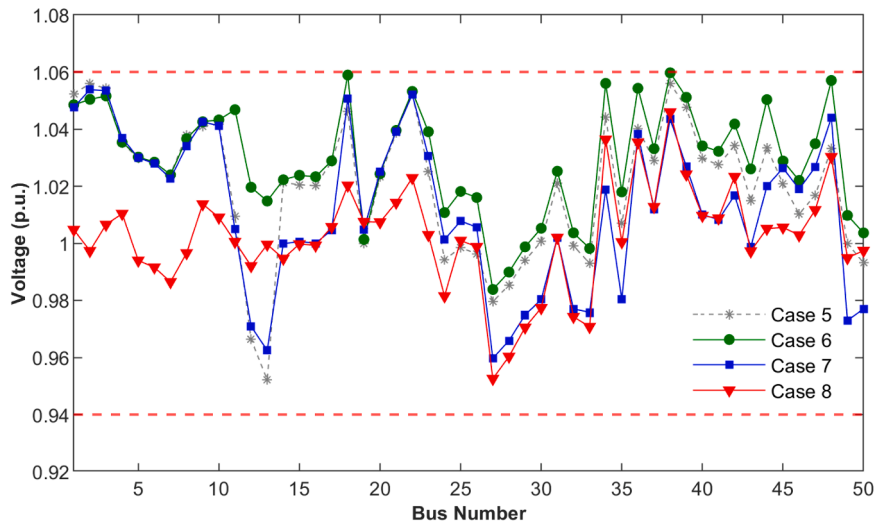
Fig. 12. Load bus voltage profiles for compromise solutions for Cases 5–8.
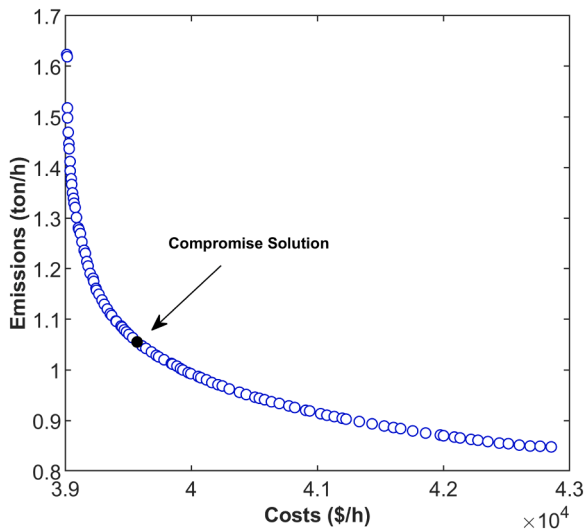
Fig. 13. Pareto front yielded by AGE-MODE for Case 5.
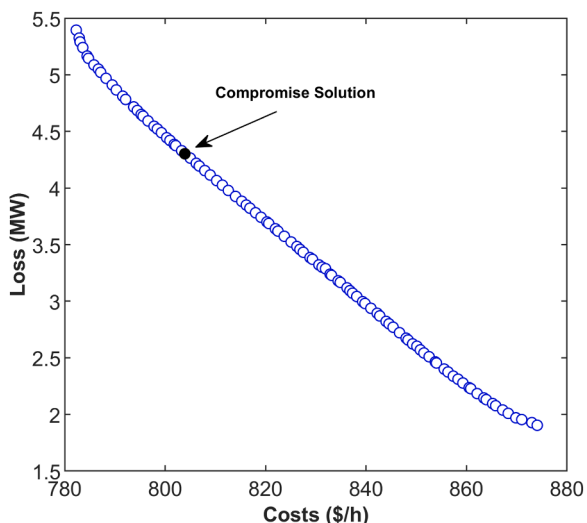

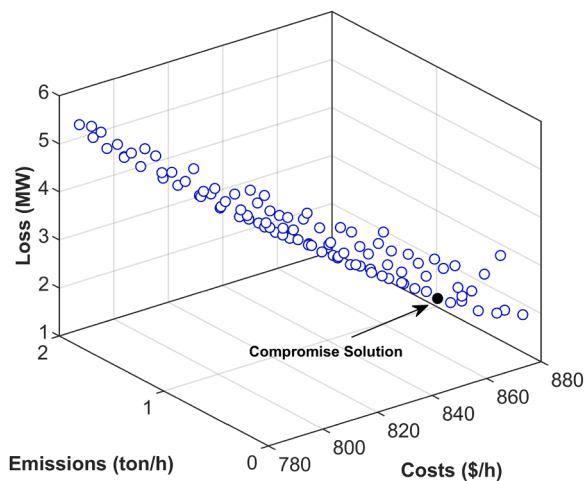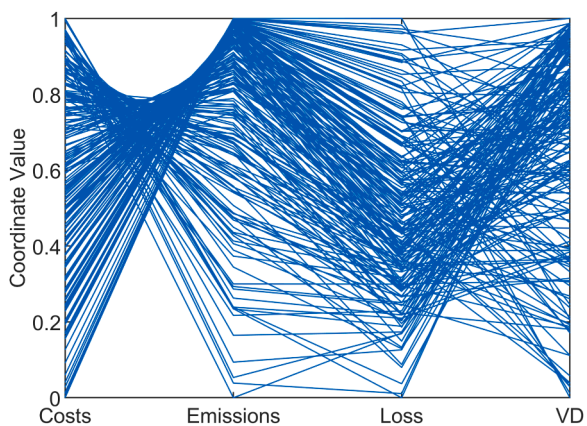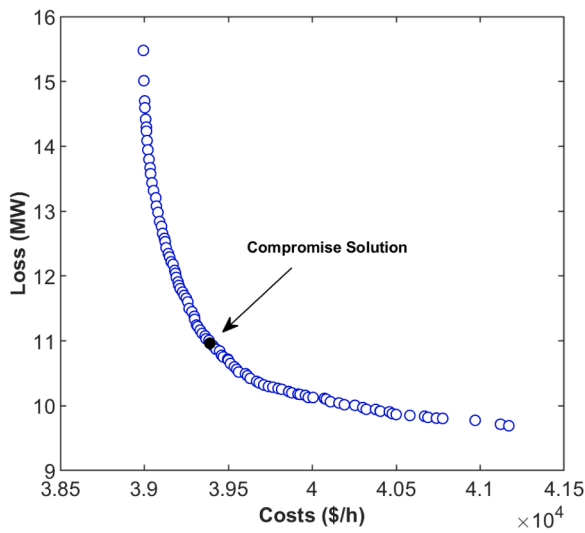**Fig. 14.** Pareto front yielded by AGE-MODE for Case 6.
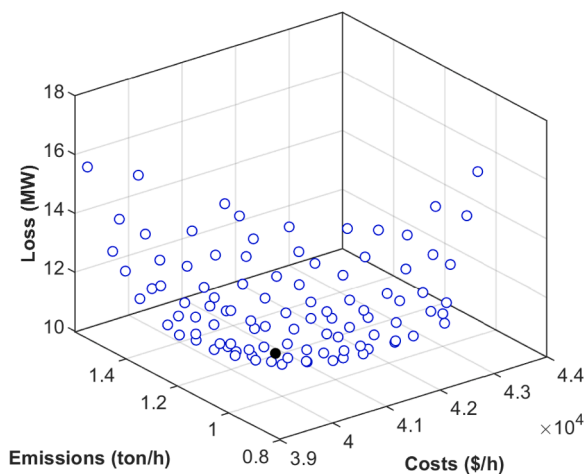
Fig. 15. Pareto front yielded by AGE-MODE for Case 7.
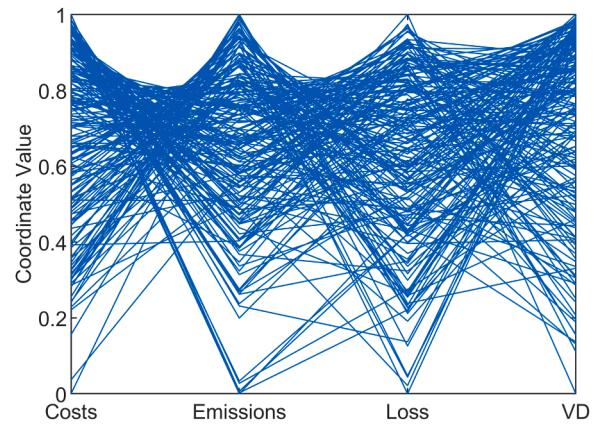
Fig. 16. Parallel coordinates plot for Pareto front yielded by AGE-MODE for Case 8.

estimating the diversity and convergence of multi-objective algorithms. An algorithm with a high hypervolume value has higher diversity and convergence performance [10]. Table 12 presents hypervolume comparisons between AGE-MODE and the other methods for all case studies. The best results for the hypervolume indicators are highlighted in Table 12. Moreover, a nonparametric Wilcoxon signed-rank test is used to statistically compare the proposed algorithm with other algorithms. As part of the statistical analysis, $R+$ represents the sum of the rankings of the runs where the proposed AGE-MODE outperforms the compared algorithm, whereas $R-$ represents the sum of the rankings for the opposite case. Wilcoxon signed-rank test is performed at a significance level of 5%. The p-value represents the significance level of the results of the statistical hypothesis test. The symbols "+" and "−" are used to indicate whether the proposed algorithm is significantly superior or inferior to other methods.

As listed in Table 12, AGE-MODE achieves the best statistical results for the hypervolume indicator in all cases. The superiority of AGE-MODE is significant for cases with more than two objective functions (Cases 3, 4, 7, and 8). This is because of the significant differences between the hypervolume values of AGE-MODE and those of the other optimizers. Based on results from the Wilcoxon Signed Ranks test, a p-value less than 0.05 and the "+" sign for all case studies indicate that AGE-MODE is significantly better than MODE, KnEA, and RPD-NSGAII. This proves that AGE-MODE outperforms the other methods in providing superior convergence and diversity for the MOOPF-TWS problem.

6. Conclusion

In this study, a robust multi-objective method, AGE-MODE, was proposed to determine the Pareto optimal solutions of a MOOPF framework integrating thermal, wind, and solar PV energy sources in a hybrid power system (MOOPF-TWS). This study has become increasingly relevant as it considers RES in light of current trends in the energy industry and environmental regulations. A new AGE-MODE was developed by combining the genetic operation of the DE method with normalization, AGE, and survival score calculation. AGE-MODE employs an AGE approach to approximate the geometry of the generated Pareto front instead of relying on assumptions such as other MOEAs. Survival scores were also applied to rank and select solutions for the next generation to strike a balance between convergence and diversity of the generated front. Hence, the proposed algorithm can significantly improve the convergence and diversity of the generated front regardless of whether it generates a Euclidean, spherical, or hyperbolic hypersurface. The MOOPF-TWS is defined as a constrained multi-objective optimization problem. Lognormal and Weibull PDFs were applied to model the uncertainties of the RESs. The total generation costs, emissions, voltage deviation, and real power loss were considered in

Table 10

Comparisons of compromise solutions between AGE-MODE and other methods for Cases 5, 6, and 7.

Algorithm	Case 5		Case 6		Case 7		
	Costs ($/h)	Emissions (ton/h)	Costs ($/h)	Loss (MW)	Costs ($/h)	Emissions (ton/h)	Loss (MW)
AGE-MODE	39569.94	**1.0552**	39390.05	**10.9636**	**40148.14**	**1.0572**	**11.0907**
MODE	39611.65	1.0773	39437.79	11.2650	40227.87	1.1439	11.8509
KnEA	39583.73	1.0593	39394.65	11.4072	40220.12	1.0669	11.2598
RPD-NSGAII	**39094.46**	1.3608	**39141.34**	12.3184	40982.58	1.0706	12.5566

Table 11

Comparison of compromise solutions between AGE-MODE and other methods for Case 8.

Algorithm	Costs ($/h)	Emissions (ton/h)	Loss (MW)	Voltage deviation (p.u.)
AGE-MODE	**40001.76**	**1.0925**	12.4100	**0.6543**
MODE	40016.56	1.2336	12.9560	0.7760
KnEA	40229.40	1.0944	**11.3313**	0.6607
RPD-NSGAII	40029.70	1.2211	13.8714	1.1838

Table 12

Comparative study of hypervolume metric between AGE-MODE and other methods.

Case study	Algorithm	HV		Wilcoxon signed-rank test			
		Average	Std.	R^+	R^-	p-value	Sig.
Case 1	AGE-MODE	**0.8418**	**0.0003**	-	-	-	
	MODE	0.8200	0.0038	465	0	1.73E-06	+
	KnEA	0.7881	0.0477	465	0	1.73E-06	+
	RPD-NSGAII	0.6989	0.0389	465	0	1.73E-06	+
Case 2	AGE-MODE	**0.6452**	**0.0010**	-	-	-	
	MODE	0.5918	0.0061	465	0	1.73E-06	+
	KnEA	0.5096	0.0507	465	0	1.73E-06	+
	RPD-NSGAII	0.5578	0.0187	465	0	1.73E-06	+
Case 3	AGE-MODE	**0.6101**	**0.0034**	-	-	-	
	MODE	0.5267	0.0125	465	0	1.73E-06	+
	KnEA	0.5491	0.0316	465	0	1.73E-06	+
	RPD-NSGAII	0.3862	0.0509	465	0	1.73E-06	+
Case 4	AGE-MODE	**0.6805**	**0.0036**	-	-	-	
	MODE	0.5971	0.0115	465	0	1.73E-06	+
	KnEA	0.6349	0.0096	465	0	1.73E-06	+
	RPD-NSGAII	0.3431	0.0747	465	0	1.73E-06	+
Case 5	AGE-MODE	**0.8669**	**0.0032**	-	-	-	
	MODE	0.8141	0.0214	465	0	1.73E-06	+
	KnEA	0.7219	0.0177	465	0	1.73E-06	+
	RPD-NSGAII	0.4890	0.0974	465	0	1.73E-06	+
Case 6	AGE-MODE	**0.8583**	**0.0192**	-	-	-	
	MODE	0.6510	0.0657	465	0	1.73E-06	+
	KnEA	0.6065	0.0563	465	0	1.73E-06	+
	RPD-NSGAII	0.6695	0.0791	465	0	1.73E-06	+
Case 7	AGE-MODE	**0.6890**	**0.0155**	-	-	-	
	MODE	0.3631	0.0646	465	0	1.73E-06	+
	KnEA	0.6037	0.0408	465	0	1.73E-06	+
	RPD-NSGAII	0.1479	0.0555	465	0	1.73E-06	+
Case 8	AGE-MODE	**0.7966**	**0.0046**	-	-	-	
	MODE	0.5750	0.0312	465	0	1.73E-06	+
	KnEA	0.7570	0.0158	465	0	1.73E-06	+
	RPD-NSGAII	0.1794	0.0436	465	0	1.73E-06	+

particular cases with combinations of two-, three-, or four-objective optimizations of modified 30-bus and 57-bus systems connected to the RES.

Detailed analyses and comparisons of the Pareto fronts, compromise solutions, and hypervolume metrics between the developed AGE-MODE and other methods were performed. The results indicated that AGE-MODE outperformed KnEA and RPD-NSGAII in terms of solution quality, convergence, and diversity characteristics. The AGE-MODE obtained better compromise solutions than the other methods for most test cases. This was further verified through statistical comparisons and Wilcoxon signed-rank test results, wherein AGE-MODE significantly outperformed the other methods in terms of the hypervolume metric for all case

studies. One highlight is that the superiority of AGE-MODE is more evident for complex cases with three- or four-objective functions. Furthermore, all system constraints are strictly satisfied, which emphasizes the effectiveness of AGE-MODE in finding feasible solutions. The high performance of AGE-MODE is owing to the efficient estimation of the shape of the optimal front for each specific case in the MOOPF-TWS problem. In summary, the proposed algorithm is suitable for solving the MOOPF-TWS framework, particularly for large-scale problems with more than two objective functions. The expansion of the MOOPF-TWS to consider battery storage systems or electric vehicle charging stations is also of significant interest. Moreover, the AGE-MODE is recommended as a solution method for multi-objective

problems in power systems.

CRediT authorship contribution statement

Truong Hoang Bao Huy: Conceptualization, Methodology, Software, Visualization, Writing – original draft and Revision. **Hien Thanh Doan**: Validation, Formal analysis, Writing – review & editing. **Dieu Ngoc Vo**: Supervision, Writing – review & editing. **Kyu-haeng Lee**: Supervision, Investigation, Writing – review & editing. **Daehee Kim**: Conceptualization, Supervision, Writing – review & editing.

Declaration of Competing Interest

The authors declare that they have no known competing financial interests or personal relationships that could have appeared to influence the work reported in this paper.

Data Availability

Data will be made available on request.

Acknowledgments

Appendix A

Table A1
IEEE 30-bus and 57-bus systems: fuel cost and emissions constants for thermal generators [42,57].

System	Generator	Bus	a	b	c	α	β	γ	ω	μ
IEEE 30-bus	TG_1	1	0	2	0.00375	0.04091	−0.05554	0.0649	0.0002	2.857
	TG_2	2	0	1.75	0.0175	0.02543	−0.06047	0.05638	0.0005	3.333
	TG_8	8	0	3.25	0.00834	0.05326	−0.0355	0.0338	0.002	2
IEEE 57-bus	TG_1	1	0	20	0.0775795	0.04	−0.05	0.06	0.00002	0.5
	TG_3	3	0	20	0.25	0.04	−0.05	0.04	0.00001	1
	TG_8	8	0	20	0.0222222	0.05	−0.05	0.045	0.00004	2
	TG_{12}	12	0	20	0.0322581	0.06	−0.05	0.05	0.00001	1.5

Appendix B

This section validates the performance of AGE-MODE using a set of well-established benchmark test problems. These benchmark test functions have diverse features obtained from the CEC2020 test suites [61]. Furthermore, the proposed AGE-MODE is compared with published results from other prominent methods employed in a previous study [36], namely MOAGDE, MO_Ring_PSO_SCD, OMNI, and NSGAII. Each test function is optimized in 21 independent trials. For fair and reliable comparisons, the initial parameters of AGE-MODE are the same as the values in [36]. The comparisons are performed based on performance indicators, including the reciprocal of hypervolume ($1/HV$), reciprocal of Pareto sets proximity ($1/PSP$), inverted generational distance in decision space ($IGDX$), and inverted generational distance in objective space ($IGDF$). Lower values of these performance metrics indicate better performance of an algorithm. Further details on the benchmark test suite and performance metrics can be found in [61].

Table B1 lists the statistical results for performance metrics of AGE-MODE and other compared methods for 24 benchmark test problems. In Table B1, the best results on the mean and standard deviation are highlighted in bold. For 24 test problems and four performance indicators, each algorithm has 96 mean values. Therefore, the ratio of the best metric values obtained by each algorithm is determined and is also presented in Table B1. These ratios are considered as a measure to evaluate the performance of algorithms. From the results in Table B1, AGE-MODE obtains the best results for 42 out of 96 metric values (i.e., 43.75%). Moreover, AGE-MODE shows extremely competitive results in the rest of the test problems. Because benchmark problems have different search spaces and complexity, no single best algorithm for all problems exists [36]. This is also confirmed in the no-free-lunch theorems [62]. Therefore, the proposed AGE-MODE achieves good performance and outperforms other algorithms for most of the CEC 2020 benchmark test functions.

Table B1
Statistical results of AGE-MODE and other methods for CEC2020 test problems.

Problem	Metric	AGE-MODE			MOAGDE			MO_Ring_PSO_SCD			OMNI			NSGAII		
		Mean	±	Std	Mean	±	Std	Mean	±	Std	Mean	±	Std	Mean	±	Std
MMF1	1/HV	**1.1433**	±	0.0001	1.1444	±	0.0002	1.1450	±	0.0002	1.1441	±	0.0008	1.1439	±	0.0008
	1/PSP	0.0324	±	0.0012	0.0278	±	0.0014	0.0297	±	0.0013	0.0491	±	0.0077	0.0702	±	0.0108
	IGDX	0.0324	±	0.0012	**0.0277**	±	0.0014	0.0296	±	0.0013	0.0487	±	0.0075	0.0693	±	0.0097
	IGDF	0.0015	±	0.0001	0.0018	±	0.0001	0.0020	±	0.0001	0.0017	±	0.0003	0.0016	±	0.0002
MMF2	1/HV	1.1710	±	0.0085	1.1664	±	0.0040	1.1692	±	0.0052	1.1636	±	0.0344	1.1558	±	0.0190
	1/PSP	0.0412	±	0.0151	0.0197	±	0.0035	0.0265	±	0.0082	0.0668	±	0.0504	0.0739	±	0.0555
	IGDX	0.0412	±	0.0151	**0.0189**	±	0.0029	0.0255	±	0.0080	0.0587	±	0.0360	0.0685	±	0.0471
	IGDF	0.0142	±	0.0033	0.0099	±	0.0008	0.0133	±	0.0028	0.0165	±	0.0297	0.0088	±	0.0122
MMF4	1/HV	1.8463	±	0.0003	1.8524	±	0.0021	1.8516	±	0.0008	1.8475	±	0.0002	1.8467	±	0.0003
	1/PSP	0.0192	±	0.0027	0.0160	±	0.0014	0.0159	±	0.0005	0.0432	±	0.0139	0.0746	±	0.0165
	IGDX	0.0192	±	0.0027	0.0159	±	0.0013	**0.0158**	±	0.0005	0.0431	±	0.0139	0.0738	±	0.0165

(continued on next page)

Table B1 (*continued*)

Problem	Metric	AGE-MODE			MOAGDE			MO_Ring_PSO_SCD			OMNI			NSGAII		
		Mean	±	Std	Mean	±	Std	Mean	±	Std	Mean	±	Std	Mean	±	Std
	IGDF	0.0012	±	0.0001	0.0018	±	0.0001	0.0018	±	0.0001	0.0014	±	0.0001	0.0013	±	0.0001
MMF5	1/HV	**1.1433**	±	0.0001	1.1445	±	0.0003	1.1449	±	0.0003	1.1438	±	0.0008	1.1433	±	0.0005
	1/PSP	0.0606	±	0.0052	0.0514	±	0.0022	0.0554	±	0.0026	0.1140	±	0.0136	0.1316	±	0.0114
	IGDX	0.0604	±	0.0052	**0.0512**	±	0.0022	0.0552	±	0.0026	0.1131	±	0.0134	0.1306	±	0.0115
	IGDF	0.0013	±	0	0.0017	±	0.0001	0.0020	±	0.0001	0.0015	±	0.0002	0.0013	±	0.0001
MMF7	1/HV	**1.1426**	±	0.0001	1.1443	±	0.0002	1.1445	±	0.0003	1.1438	±	0.0002	1.1432	±	0.0003
	1/PSP	**0.0148**	±	0.0012	0.0150	±	0.0008	0.0159	±	0.0007	0.0248	±	0.0056	0.0469	±	0.0077
	IGDX	**0.0147**	±	0.0012	0.0149	±	0.0007	0.0159	±	0.0007	0.0247	±	0.0055	0.0465	±	0.0075
	IGDF	**0.0011**	±	0.0001	0.0017	±	0.0001	0.0018	±	0.0001	0.0015	±	0.0001	0.0013	±	0.0001
MMF8	1/HV	2.3664	±	0.0016	2.4100	±	0.0280	2.3889	±	0.0161	2.3646	±	0.0004	2.3633	±	0.0003
	1/PSP	0.0838	±	0.0215	0.0692	±	0.0129	0.0406	±	0.0022	0.1646	±	0.0978	0.6662	±	0.2763
	IGDX	0.0812	±	0.0198	0.0673	±	0.0122	**0.0404**	±	0.0021	0.1609	±	0.0963	0.5517	±	0.2067
	IGDF	0.0013	±	0	0.0029	±	0.0002	0.0028	±	0.0002	0.0016	±	0.0001	0.0013	±	0.0001
MMF10	1/HV	**0.0777**	±	0	0.0795	±	0.0006	0.0796	±	0.0006	0.0797	±	0.0025	0.0820	±	0.0031
	1/PSP	**0.0020**	±	0.0001	0.0233	±	0.0081	0.0280	±	0.0170	0.0889	±	0.0915	0.1913	±	0.1362
	IGDX	**0.0020**	±	0.0001	0.0223	±	0.0068	0.0264	±	0.0141	0.0823	±	0.0881	0.1875	±	0.1375
	IGDF	0.0065	±	0.0004	0.0918	±	0.0188	0.1012	±	0.0377	0.1004	±	0.0981	0.1850	±	0.1078
MMF11	1/HV	**0.0688**	±	0	0.0689	±	0	0.0690	±	0	0.0689	±	0	0.0689	±	0
	1/PSP	**0.0026**	±	0.0001	0.0051	±	0.0004	0.0055	±	0.0004	0.0043	±	0.0003	0.0036	±	0.0004
	IGDX	**0.0026**	±	0.0001	0.0051	±	0.0004	0.0055	±	0.0004	0.0043	±	0.0003	0.0036	±	0.0004
	IGDF	**0.0092**	±	0.0005	0.0145	±	0.0011	0.0183	±	0.0014	0.0122	±	0.0016	0.0110	±	0.0005
MMF12	1/HV	**0.6354**	±	0.0000	0.6385	±	0.0008	0.6394	±	0.0019	0.6366	±	0.0030	0.6362	±	0.0019
	1/PSP	**0.0014**	±	0.0001	0.0044	±	0.0006	0.0039	±	0.0004	0.0028	±	0.0022	0.0022	±	0.0012
	IGDX	**0.0014**	±	0.0001	0.0044	±	0.0006	0.0039	±	0.0004	0.0028	±	0.0022	0.0022	±	0.0012
	IGDF	**0.0020**	±	0.0001	0.0069	±	0.0008	0.0073	±	0.0013	0.0036	±	0.0040	0.0027	±	0.0014
MMF13	1/HV	**0.0542**	±	0	0.0544	±	0	0.0545	±	0.0001	0.0543	±	0	0.0542	±	0
	1/PSP	0.0378	±	0.0052	0.0365	±	0.0027	0.0373	±	0.0024	0.0708	±	0.0148	0.1046	±	0.0318
	IGDX	0.0377	±	0.0051	**0.0361**	±	0.0026	0.0368	±	0.0024	0.0680	±	0.0115	0.0876	±	0.0147
	IGDF	0.0116	±	0.0002	0.0263	±	0.0030	0.0325	±	0.0047	0.0154	±	0.0011	0.0138	±	0.0007
MMF14	1/HV	0.3511	±	0.0090	0.3855	±	0.0685	0.3561	±	0.0224	0.3348	±	0.0071	0.3543	±	0.0063
	1/PSP	0.0458	±	0.0029	0.0486	±	0.0016	0.0466	±	0.0013	0.0795	±	0.0051	0.0961	±	0.0125
	IGDX	**0.0458**	±	0.0029	0.0486	±	0.0016	0.0466	±	0.0013	0.0795	±	0.0051	0.0961	±	0.0125
	IGDF	**0.0493**	±	0.0010	0.0664	±	0.0020	0.0687	±	0.0012	0.0847	±	0.0031	0.0987	±	0.0056
MMF15	1/HV	**0.2366**	±	0.0047	0.2464	±	0.0118	0.2468	±	0.0162	0.2422	±	0.0119	0.2384	±	0.0061
	1/PSP	**0.0401**	±	0.0010	0.0499	±	0.0022	0.0511	±	0.0019	0.0704	±	0.0056	0.0745	±	0.0083
	IGDX	**0.0401**	±	0.0010	0.0499	±	0.0022	0.0511	±	0.0019	0.0704	±	0.0056	0.0745	±	0.0083
	IGDF	**0.0726**	±	0.0010	0.0995	±	0.0049	0.1067	±	0.0054	0.1390	±	0.0109	0.1433	±	0.0124
MMF1_e	1/HV	**1.1464**	±	0.0019	1.2504	±	0.0985	1.1681	±	0.0114	1.1534	±	0.0084	1.1572	±	0.0118
	1/PSP	1.6231	±	1.0374	0.2712	±	0.0337	0.3840	±	0.1030	1.3824	±	0.8527	2.4469	±	1.6908
	IGDX	1.0625	±	0.5114	**0.2619**	±	0.0288	0.3449	±	0.0751	0.9569	±	0.5053	1.4149	±	0.5492
	IGDF	0.0026	±	0.0002	0.0093	±	0.0010	0.0075	±	0.0007	0.0061	±	0.0071	0.0084	±	0.0070
MMF14_a	1/HV	0.3485	±	0.0105	0.3597	±	0.0237	0.3327	±	0.0325	0.3268	±	0.0099	0.3467	±	0.0068
	1/PSP	0.0646	±	0.0034	0.0568	±	0.0020	0.0529	±	0.0012	0.0974	±	0.0086	0.1243	±	0.0141
	IGDX	0.0646	±	0.0034	0.0567	±	0.0020	**0.0528**	±	0.0012	0.0974	±	0.0086	0.1243	±	0.0141
	IGDF	0.0504	±	0.0011	0.0665	±	0.0015	0.0673	±	0.0015	0.0912	±	0.0030	0.1042	±	0.0072
MMF15_a	1/HV	0.2370	±	0.0051	0.2484	±	0.0130	0.2401	±	0.0149	0.2358	±	0.0092	0.2396	±	0.0078
	1/PSP	0.0499	±	0.0017	0.0581	±	0.0029	0.0553	±	0.0019	0.0896	±	0.0076	0.1045	±	0.0117
	IGDX	**0.0499**	±	0.0017	0.0579	±	0.0029	0.0552	±	0.0019	0.0896	±	0.0076	0.1045	±	0.0117
	IGDF	**0.0751**	±	0.0012	0.1035	±	0.0051	0.1037	±	0.0039	0.1444	±	0.0134	0.1573	±	0.0131
MMF10_l	1/HV	**0.0776**	±	0	0.0786	±	0.0002	0.0789	±	0.0003	0.0792	±	0.0027	0.0787	±	0.0024
	1/PSP	7.9653	±	0.6365	0.1731	±	0.0093	0.1747	±	0.0090	5.7899	±	4.1137	7.2508	±	3.8691
	IGDX	0.2005	±	0	0.1690	±	0.0078	**0.1677**	±	0.0027	0.1936	±	0.0340	0.1950	±	0.0192
	IGDF	0.1925	±	0.0001	0.1706	±	0.0086	0.1809	±	0.0104	0.1933	±	0.0322	0.1946	±	0.0205
MMF11_l	1/HV	0.0688	±	0	0.0689	±	0	0.0689	±	0	0.0688	±	0	0.0688	±	0
	1/PSP	3.6812	±	0.9552	0.5072	±	0.5022	0.7133	±	0.5669	2.1163	±	0.0605	3.4516	±	0.8072
	IGDX	0.2509	±	0.0001	**0.2130**	±	0.0239	0.2211	±	0.0254	0.2500	±	0.0002	0.2509	±	0.0003
	IGDF	0.0911	±	0.0002	**0.0782**	±	0.0064	0.0814	±	0.0072	0.0918	±	0.0003	0.0915	±	0.0002
MMF12_l	1/HV	0.6352	±	0	0.6365	±	0.0004	0.6377	±	0.0014	0.6353	±	0	0.6352	±	0
	1/PSP	2.7569	±	0.2219	0.6968	±	0.5556	0.6401	±	0.5543	2.5924	±	0.1749	2.2789	±	0.0001
	IGDX	0.2457	±	0.0002	0.2053	±	0.0385	**0.1968**	±	0.0425	0.2462	±	0.0003	0.2470	±	0.0005
	IGDF	0.0824	±	0.0002	0.0656	±	0.0117	**0.0634**	±	0.0142	0.0822	±	0	0.0822	±	0.0001
MMF13_l	1/HV	0.0542	±	0	0.0543	±	0	0.0543	±	0	0.0542	±	0	0.0542	±	0
	1/PSP	0.5438	±	0.0047	0.3735	±	0.0958	0.3292	±	0.0853	0.5926	±	0.0141	0.6688	±	0.0996
	IGDX	0.2561	±	0.0019	0.2370	±	0.0141	**0.2274**	±	0.0145	0.2806	±	0.0066	0.2918	±	0.0113
	IGDF	0.1442	±	0.0004	0.0896	±	0.0232	**0.0876**	±	0.0137	0.1449	±	0.0009	0.1447	±	0.0009
MMF15_l	1/HV	0.2368	±	0.0026	0.2441	±	0.0112	0.2357	±	0.0080	0.2339	±	0.0054	0.2366	±	0.0046
	1/PSP	0.5913	±	0.0887	0.1488	±	0.0147	0.1516	±	0.0178	0.3772	±	0.1399	0.4482	±	0.2009
	IGDX	0.2599	±	0.0017	**0.1487**	±	0.0147	0.1515	±	0.0178	0.2491	±	0.0185	0.2583	±	0.0187
	IGDF	0.1745	±	0.0035	**0.1621**	±	0.0046	0.1652	±	0.0027	0.1960	±	0.0054	0.2036	±	0.0090
MMF15_a_l	1/HV	0.2353	±	0.0037	0.2470	±	0.0082	0.2327	±	0.0074	0.2320	±	0.0083	0.2340	±	0.0046
	1/PSP	0.2612	±	0.0040	0.1560	±	0.0137	0.1689	±	0.0179	0.2474	±	0.0332	0.2758	±	0.0268
	IGDX	0.2114	±	0.0023	**0.1527**	±	0.0119	0.1651	±	0.0152	0.2150	±	0.0147	0.2291	±	0.0092
	IGDF	0.1704	±	0.0027	**0.1601**	±	0.0047	0.1665	±	0.0024	0.1994	±	0.0071	0.2024	±	0.0100
MMF16_l1	1/HV	0.2342	±	0.0023	0.2453	±	0.0133	0.2323	±	0.0068	0.2274	±	0.0031	0.2349	±	0.0023

Table B1 (*continued*)

Problem	Metric	AGE-MODE			MOAGDE			MO_Ring_PSO_SCD			OMNI			NSGAII		
		Mean	±	Std	Mean	±	Std	Mean	±	Std	Mean	±	Std	Mean	±	Std
	1/PSP	0.1929	±	0.0074	0.1035	±	0.0075	0.1053	±	0.0082	0.1944	±	0.0295	0.2179	±	0.0340
	IGDX	0.1482	±	0.0010	**0.1035**	±	0.0075	0.1053	±	0.0082	0.1656	±	0.0058	0.1768	±	0.0085
	IGDF	0.1309	±	0.0026	**0.1267**	±	0.0033	0.1290	±	0.0024	0.1496	±	0.0049	0.1648	±	0.0060
MMF16_l2	1/HV	0.2338	±	0.0036	0.2441	±	0.0099	0.2303	±	0.0083	0.2302	±	0.0059	0.2343	±	0.0030
	1/PSP	0.7897	±	0.1182	0.1838	±	0.0242	0.2036	±	0.0290	0.5537	±	0.1787	0.4563	±	0.1961
	IGDX	0.3321	±	0.0026	**0.1820**	±	0.0209	0.2023	±	0.0277	0.3169	±	0.0224	0.3169	±	0.0145
	IGDF	0.2267	±	0.0044	**0.1972**	±	0.0046	0.2026	±	0.0057	0.2316	±	0.0065	0.2383	±	0.0052
MMF16_l3	1/HV	0.2340	±	0.0022	0.2411	±	0.0112	0.2315	±	0.0078	0.2281	±	0.0042	0.2345	±	0.0025
	1/PSP	0.2776	±	0.0160	0.1409	±	0.0120	0.1417	±	0.0106	0.2826	±	0.0363	0.2724	±	0.0427
	IGDX	0.2016	±	0.0021	**0.1409**	±	0.0120	0.1414	±	0.0101	0.2157	±	0.0051	0.2198	±	0.0086
	IGDF	0.1772	±	0.0034	0.1613	±	0.0047	0.1604	±	0.0033	0.1870	±	0.0039	0.1983	±	0.0062
Overall		42/96			30/42			14/96			10/96			12/96		

References

[1] P.P. Biswas, P.N. Suganthan, R. Mallipeddi, G.A.J. Amaratunga, Optimal power flow solutions using differential evolution algorithm integrated with effective constraint handling techniques, Eng. Appl. Artif. Intell. 68 (2018) 81–100, https://doi.org/10.1016/j.engappai.2017.10.019.

[2] S. Li, W. Gong, L. Wang, X. Yan, C. Hu, Optimal power flow by means of improved adaptive differential evolution, Energy 198 (2020), 117314, https://doi.org/10.1016/j.energy.2020.117314.

[3] S. Li, W. Gong, C. Hu, X. Yan, L. Wang, Q. Gu, Adaptive constraint differential evolution for optimal power flow, Energy 235 (2021), 121362, https://doi.org/10.1016/j.energy.2021.121362.

[4] A.-A.A. Mohamed, Y.S. Mohamed, A.A.M. El-Gaafary, A.M. Hemeida, Optimal power flow using moth swarm algorithm, Electr. Power Syst. Res. 142 (2017) 190–206, https://doi.org/10.1016/j.epsr.2016.09.025.

[5] B. Bentouati, A. Khelifi, A.M. Shaheen, R.A. El-Sehiemy, An enhanced moth-swarm algorithm for efficient energy management based multi dimensions OPF problem, J. Ambient Intell. Hum. Comput. 12 (2021) 9499–9519, https://doi.org/10.1007/s12652-020-02692-7.

[6] K. Srilakshmi, P. Ravi Babu, P. Aravindhababu, An enhanced most valuable player algorithm based optimal power flow using Broyden's method, Sustain. Energy Technol. Assess. 42 (2020), 100801, https://doi.org/10.1016/j.seta.2020.100801.

[7] P. Pravina, M.R. Babu, A.R. Kumar, Solving optimal power flow problems using adaptive quasi-oppositional differential migrated biogeography-based optimization, J. Electr. Eng. Technol. 16 (2021) 1891–1903, https://doi.org/10.1007/s42835-021-00739-z.

[8] A. Meng, C. Zeng, P. Wang, D. Chen, T. Zhou, X. Zheng, H. Yin, A high-performance crisscross search based grey wolf optimizer for solving optimal power flow problem, Energy 225 (2021), 120211, https://doi.org/10.1016/j.energy.2021.120211.

[9] S. Abd el-sattar, S. Kamel, M. Ebeed, F. Jurado, An improved version of salp swarm algorithm for solving optimal power flow problem, Soft Comput. 25 (2021) 4027–4052, https://doi.org/10.1007/s00500-020-05431-4.

[10] T.H.B. Huy, P. Nallagownden, K.H. Truong, R. Kannan, D.N. Vo, N. Ho, Multi-objective search group algorithm for engineering design problems, Appl. Soft Comput. 126 (2022), 109287, https://doi.org/10.1016/j.asoc.2022.109287.

[11] T.H.B. Huy, D. Kim, D.N. Vo, Multiobjective optimal power flow using multiobjective search group algorithm, IEEE Access 10 (2022) 77837–77856, https://doi.org/10.1109/ACCESS.2022.3193371.

[12] J. Zhang, S. Wang, Q. Tang, Y. Zhou, T. Zeng, An improved NSGA-III integrating adaptive elimination strategy to solution of many-objective optimal power flow problems, Energy 172 (2019) 945–957, https://doi.org/10.1016/j.energy.2019.02.009.

[13] R.A. El Sehiemy, F. Selim, B. Bentouati, M.A. Abido, A novel multi-objective hybrid particle swarm and salp optimization algorithm for technical-economical-environmental operation in power systems, Energy 193 (2020), 116817, https://doi.org/10.1016/j.energy.2019.116817.

[14] J. Qian, P. Wang, C. Pu, G. Chen, Joint application of multi-object beetle antennae search algorithm and BAS-BP fuel cost forecast network on optimal active power dispatch problems, Knowl. -Based Syst. 226 (2021), 107149, https://doi.org/10.1016/j.knosys.2021.107149.

[15] A.M. Shaheen, R.A. El-Sehiemy, M.M. Alharthi, S.S.M. Ghoneim, A.R. Ginidi, Multi-objective jellyfish search optimizer for efficient power system operation based on multi-dimensional OPF framework, Energy 237 (2021) 121478, https://doi.org/10.1016/j.energy.2021.121478.

[16] P.P. Biswas, P.N. Suganthan, R. Mallipeddi, G.A.J. Amaratunga, Multi-objective optimal power flow solutions using a constraint handling technique of evolutionary algorithms, Soft Comput. 24 (2020) 2999–3023, https://doi.org/10.1007/s00500-019-04077-1.

[17] A.M. Shaheen, R.A. El-Sehiemy, H.M. Hasanien, A.R. Ginidi, An improved heap optimization algorithm for efficient energy management based optimal power flow model, Energy 250 (2022), 123795, https://doi.org/10.1016/j.energy.2022.123795.

[18] J. Qian, P. Wang, C. Pu, X. Peng, G. Chen, Application of modified beetle antennae search algorithm and BP power flow prediction model on multi-objective optimal active power dispatch, Appl. Soft Comput. 113 (2021), 108027, https://doi.org/10.1016/j.asoc.2021.108027.

[19] H.T. Kahraman, M. Akbel, S. Duman, Optimization of optimal power flow problem using multi-objective manta ray foraging optimizer, Appl. Soft Comput. 116 (2022), 108334, https://doi.org/10.1016/j.asoc.2021.108334.

[20] P.P. Biswas, P.N. Suganthan, G.A.J. Amaratunga, Optimal power flow solutions incorporating stochastic wind and solar power, Energy Convers. Manag. 148 (2017) 1194–1207, https://doi.org/10.1016/j.enconman.2017.06.071.

[21] Z. Ullah, S. Wang, J. Radosavljević, J. Lai, A solution to the optimal power flow problem considering WT and PV generation, IEEE Access 7 (2019) 46763–46772, https://doi.org/10.1109/ACCESS.2019.2909561.

[22] E.E. Elattar, Optimal power flow of a power system incorporating stochastic wind power based on modified moth swarm algorithm, IEEE Access 7 (2019) 89581–89593, https://doi.org/10.1109/ACCESS.2019.2927193.

[23] S. Duman, J. Li, L. Wu, U. Guvenc, Optimal power flow with stochastic wind power and FACTS devices: a modified hybrid PSOGSA with chaotic maps approach, Neural Comput. Applic 32 (2020) 8463–8492, https://doi.org/10.1007/s00521-019-04338-y.

[24] J. Ben Hmida, T. Chambers, J. Lee, Solving constrained optimal power flow with renewables using hybrid modified imperialist competitive algorithm and sequential quadratic programming, Electr. Power Syst. Res. 177 (2019), 105989, https://doi.org/10.1016/j.epsr.2019.105989.

[25] S. Duman, S. Rivera, J. Li, L. Wu, Optimal power flow of power systems with controllable wind-photovoltaic energy systems via differential evolutionary particle swarm optimization, Int. Trans. Electr. Energy Syst. 30 (2020), e12270, https://doi.org/10.1002/2050-7038.12270.

[26] U. Guvenc, S. Duman, H.T. Kahraman, S. Aras, M. Katı, Fitness–Distance Balance based adaptive guided differential evolution algorithm for security-constrained optimal power flow problem incorporating renewable energy sources, Appl. Soft Comput. 108 (2021), 107421, https://doi.org/10.1016/j.asoc.2021.107421.

[27] E. Kaymaz, S. Duman, U. Guvenc, Optimal power flow solution with stochastic wind power using the Lévy coyote optimization algorithm, Neural Comput. Applic 33 (2021) 6775–6804, https://doi.org/10.1007/s00521-020-05455-9.

[28] M.H. Sulaiman, Z. Mustaffa, Solving optimal power flow problem with stochastic wind–solar–small hydro power using barnacles mating optimizer, Control Eng. Pract. 106 (2021), 104672, https://doi.org/10.1016/j.conengprac.2020.104672.

[29] M. Rawa, A. Abusorrah, H. Bassi, S. Mekhilef, Z.M. Ali, S.H.E. Abdel Aleem, H.M. Hasanien, A.I. Omar, Economical-technical-environmental operation of power networks with wind-solar-hydropower generation using analytic hierarchy process and improved grey wolf algorithm, Ain Shams Eng. J. 12 (2021) 2717–2734, https://doi.org/10.1016/j.asej.2021.02.004.

[30] S. Duman, H.T. Kahraman, M. Kati, Economical operation of modern power grids incorporating uncertainties of renewable energy sources and load demand using the adaptive fitness-distance balance-based stochastic fractal search algorithm, Eng. Appl. Artif. Intell. 117 (2023), 105501, https://doi.org/10.1016/j.engappai.2022.105501.

[31] M. Ebeed, A. Mostafa, M.M. Aly, F. Jurado, S. Kamel, Stochastic optimal power flow analysis of power systems with wind/PV/ TCSC using a developed Runge Kutta optimizer, Int. J. Electr. Power Energy Syst. 152 (2023), 109250, https://doi.org/10.1016/j.ijepes.2023.109250.

[32] A. Man-Im, W. Ongsakul, J.G. Singh, M.N. Madhu, Multi-objective optimal power flow considering wind power cost functions using enhanced PSO with chaotic mutation and stochastic weights, Electr. Eng. 101 (2019) 699–718, https://doi.org/10.1007/s00202-019-00815-8.

[33] S.R. Salkuti, Optimal power flow using multi-objective glowworm swarm optimization algorithm in a wind energy integrated power system, Int. J. Green. Energy 16 (2019) 1547–1561, https://doi.org/10.1080/15435075.2019.1677234.

[34] P.P. Biswas, P.N. Suganthan, B.Y. Qu, G.A.J. Amaratunga, Multiobjective economic-environmental power dispatch with stochastic wind-solar-small hydro power, Energy 150 (2018) 1039–1057, https://doi.org/10.1016/j.energy.2018.03.002.

[35] M.-R. Chen, G.-Q. Zeng, K.-D. Lu, Constrained multi-objective population extremal optimization based economic-emission dispatch incorporating renewable energy resources, Renew. Energy 143 (2019) 277–294, https://doi.org/10.1016/j.renene.2019.05.024.

[36] S. Duman, M. Akbel, H.T. Kahraman, Development of the multi-objective adaptive guided differential evolution and optimization of the MO-ACOPF for wind/PV/tidal energy sources, Appl. Soft Comput. 112 (2021), 107814, https://doi.org/10.1016/j.asoc.2021.107814.

[37] S. Li, W. Gong, L. Wang, Q. Gu, Multi-objective optimal power flow with stochastic wind and solar power, Appl. Soft Comput. 114 (2022), 108045, https://doi.org/10.1016/j.asoc.2021.108045.

[38] T.H.B. Huy, T.P. Nguyen, N. Mohd Nor, I. Elamvazuthi, T. Ibrahim, D.N. Vo, Performance improvement of multiobjective optimal power flow-based renewable energy sources using intelligent algorithm, IEEE Access 10 (2022) 48379–48404, https://doi.org/10.1109/ACCESS.2022.3170547.

[39] D. Lv, G. Xiong, X. Fu, Economic emission dispatch of power systems considering solar uncertainty with extended multi-objective differential evolution, Expert Syst. Appl. 227 (2023) 120298, https://doi.org/10.1016/j.eswa.2023.120298.

[40] N. Li, G. Zhou, Y. Zhou, W. Deng, Q. Luo, Multi-objective pathfinder algorithm for multi-objective optimal power flow problem with random renewable energy sources: wind, photovoltaic and tidal, Sci. Rep. 13 (2023), 10647, https://doi.org/10.1038/s41598-023-37635-7.

[41] A. Panichella, An adaptive evolutionary algorithm based on non-euclidean geometry for many-objective optimization (New York, NY, USA), : Proc. Genet. Evolut. Comput. Conf., Assoc. Comput. Mach. (2019) 595–603, https://doi.org/10.1145/3321707.3321839.

[42] A.E. Chaib, H.R.E.H. Bouchekara, R. Mehasni, M.A. Abido, Optimal power flow with emission and non-smooth cost functions using backtracking search optimization algorithm, Int. J. Electr. Power Energy Syst. 81 (2016) 64–77, https://doi.org/10.1016/j.ijepes.2016.02.004.

[43] H.R.E.H. Bouchekara, A.E. Chaib, M.A. Abido, R.A. El-Sehiemy, Optimal power flow using an Improved Colliding Bodies Optimization algorithm, Appl. Soft Comput. 42 (2016) 119–131, https://doi.org/10.1016/j.asoc.2016.01.041.

[44] C.-L. Chen, T.-Y. Lee, R.-M. Jan, Optimal wind-thermal coordination dispatch in isolated power systems with large integration of wind capacity, Energy Convers. Manag. 47 (2006) 3456–3472, https://doi.org/10.1016/j.enconman.2005.12.016.

[45] S.S. Reddy, P.R. Bijwe, A.R. Abhyankar, Real-time economic dispatch considering renewable power generation variability and uncertainty over scheduling period, IEEE Syst. J. 9 (2015) 1440–1451, https://doi.org/10.1109/JSYST.2014.2325967.

[46] S.S. Reddy, Optimal scheduling of thermal-wind-solar power system with storage, Renew. Energy 101 (2017) 1357–1368, https://doi.org/10.1016/j.renene.2016.10.022.

[47] P.P. Biswas, P. Arora, R. Mallipeddi, P.N. Suganthan, B.K. Panigrahi, Optimal placement and sizing of FACTS devices for optimal power flow in a wind power integrated electrical network, Neural Comput. Applic 33 (2021) 6753–6774, https://doi.org/10.1007/s00521-020-05453-x.

[48] T.-P. Chang, Investigation on frequency distribution of global radiation using different probability density functions, Int. J. Appl. Sci. Eng. 8 (2010) 99–107, https://doi.org/10.6703/IJASE.2010.8(2).99.

[49] M.A. Abido, Environmental/economic power dispatch using multiobjective evolutionary algorithms, IEEE Trans. Power Syst. 18 (2003) 1529–1537, https://doi.org/10.1109/TPWRS.2003.818693.

[50] R. Storn, K. Price, Differential evolution – a simple and efficient heuristic for global optimization over continuous spaces, J. Glob. Optim. 11 (1997) 341–359, https://doi.org/10.1023/A:1008202821328.

[51] K. Deb, A. Pratap, S. Agarwal, T. Meyarivan, A fast and elitist multiobjective genetic algorithm: NSGA-II, IEEE Trans. Evolut. Comput. 6 (2002) 182–197, https://doi.org/10.1109/4235.996017.

[52] K. Deb, H. Jain, An evolutionary many-objective optimization algorithm using reference-point-based nondominated sorting approach, part I: solving problems with box constraints, IEEE Trans. Evolut. Comput. 18 (2014) 577–601, https://doi.org/10.1109/TEVC.2013.2281535.

[53] H. Jain, K. Deb, An evolutionary many-objective optimization algorithm using reference-point based nondominated sorting approach, part II: handling constraints and extending to an adaptive approach, IEEE Trans. Evolut. Comput. 18 (2014) 602–622, https://doi.org/10.1109/TEVC.2013.2281534.

[54] A.C. Thompson, Minkowski Geometry, Cambridge University Press, Cambridge, 1996, https://doi.org/10.1017/CBO9781107325845.

[55] R.D. Zimmerman, C.E. Murillo-Sanchez, MATPOWER-manual-4.1.pdf, Power Systems Engineering Research Center, Cornell University, Ithaca, NY, 2011. ⟨https://matpower.org/docs/MATPOWER-manual-4.1.pdf⟩ (accessed September 19, 2020).

[56] W. Sheng, K.-Y. Liu, Y. Liu, X. Meng, Y. Li, Optimal placement and sizing of distributed generation via an improved nondominated sorting genetic algorithm II, IEEE Trans. Power Deliv. 30 (2015) 569–578, https://doi.org/10.1109/TPWRD.2014.2325938.

[57] O. Alsac, B. Stott, Optimal load flow with steady-state security, IEEE Trans. Power Appar. Syst. PAS- 93 (1974) 745–751, https://doi.org/10.1109/TPAS.1974.293972.

[58] X. Zhang, Y. Tian, Y. Jin, A knee point-driven evolutionary algorithm for many-objective optimization, IEEE Trans. Evolut. Comput. 19 (2015) 761–776, https://doi.org/10.1109/TEVC.2014.2378512.

[59] M. Elarbi, S. Bechikh, A. Gupta, L. Ben Said, Y.-S. Ong, A new decomposition-based NSGA-II for many-objective optimization, IEEE Trans. Syst., Man, Cybern.: Syst. 48 (2018) 1191–1210, https://doi.org/10.1109/TSMC.2017.2654301.

[60] K. Deb, Multi-Objective Optimization Using Evolutionary Algorithms, John Wiley & Sons, Inc, USA, 2001.

[61] J. Liang, P. Suganthan, B. Qu, D. Gong, C. Yue, Problem Definitions and Evaluation Criteria for the CEC 2020 Special Session on Multimodal Multiobjective Optimization, 2019. https://doi.org/10.13140/RG.2.2.31746.02247.

[62] D.H. Wolpert, W.G. Macready, No free lunch theorems for optimization, IEEE Trans. Evolut. Comput. 1 (1997) 67–82, https://doi.org/10.1109/4235.585893.